Published online 8 February 2022

Nucleic Acids Research, 2022, Vol. 50, No. 12 ***6601–6617***
https://doi.org/10.1093/nar/gkac053

NAR Breakthrough Article

Deficiency of ribosomal proteins reshapes the transcriptional and translational landscape in human cells

Yizhao Luan[1,†], Nan Tang[1,†], Jiaqi Yang[1,†], Shuting Liu[1], Chichi Cheng[2], Yan Wang[1], Congying Chen[1], Ya-nan Guo[1], Hongwei Wang[1], Wenxue Zhao[2], Qian Zhao[3], Wei Li[4], Mengqing Xiang[1], Rong Ju[1,*] and Zhi Xie[1,5,*]

[1]State Key Laboratory of Ophthalmology, Zhongshan Ophthalmic Center, Sun Yat-sen University, Guangzhou, China, [2]School of Medicine, Sun Yat-Sen University, Guangzhou, China, [3]State Key Laboratory of Chemical Biology and Drug Discovery, Department of Applied Biology and Chemical Technology, Hong Kong Polytechnic University, Hong Kong SAR 999077, China, [4]Retinal Neurophysiology Section, National Eye Institute, National Institutes of Health, Bethesda, MD 20892, USA and [5]Center for Precision Medicine, Sun Yat-sen University, Guangzhou, China

Received July 08, 2021; Revised January 13, 2022; Editorial Decision January 14, 2022; Accepted February 03, 2022

ABSTRACT

Human ribosomes have long been thought to be uniform factories with little regulatory function. Accumulating evidence emphasizes the heterogeneity of ribosomal protein (RP) expression in specific cellular functions and development. However, a systematic understanding of functional relevance of RPs is lacking. Here, we surveyed translational and transcriptional changes after individual knockdown of 75 RPs, 44 from the large subunit (60S) and 31 from the small subunit (40S), by Ribo-seq and RNA-seq analyses. Deficiency of individual RPs altered specific subsets of genes transcriptionally and translationally. RP genes were under cotranslational regulation upon ribosomal stress, and deficiency of the 60S RPs and the 40S RPs had opposite effects. RP deficiency altered the expression of genes related to eight major functional classes, including the cell cycle, cellular metabolism, signal transduction and development. 60S RP deficiency led to greater inhibitory effects on cell growth than did 40S RP deficiency, through P53 signaling. Particularly, we showed that *eS8*/*RPS8* deficiency stimulated apoptosis while *eL13*/*RPL13* or *eL18*/*RPL18* deficiency promoted senescence. We also validated the phenotypic impacts of *uL5*/*RPL11* and *eL15*/*RPL15* deficiency on retina development and angiogenesis, respectively. Overall, our study provides a valuable resource for and novel insights into ribosome regulation in cellular activities, development and diseases.

INTRODUCTION

Human ribosomes are complex cellular machines consisting of ∼80 ribosomal proteins (RPs) and four ribosomal RNAs (rRNAs) and are the main effectors of protein synthesis, a process termed translation (1). The majority of RPs sequentially assemble with rRNAs into evolutionarily conserved structures containing ribosomal functional modules and key architectural features, such as the small (40S) and large (60S) subunits (2–4). Despite the variety of changes in the abundances and modifications of RPs and rRNAs (5), ribosomes have long been thought to be compositionally passive uniform molecular factories with few regulatory roles. Recent advances in mass spectrometry and high-throughput (HT) analysis have begun to allow the distinct stoichiometry and functional heterogeneity of RPs to be characterized in mammalian systems.

RP genes are differentially expressed across different normal tissues, cell types and cancers. For instance, HT quantification of human RPs revealed their tissue-specific expression pattern at the mRNA level in normal tissues (6). Different RPs, such as *uL1*/*Rpl10a*, *eL38*/*Rpl38*, *eS7*/*Rps7* and *eS25*/*Rps25*, exhibit varying stoichiometry in polysomes in mouse embryonic stem cells (7). Whereas hemizygous

*To whom correspondence should be addressed. Tel: +86 02 6667 7086; Email: xiezhi@gmail.com
Correspondence may also be addressed to Rong Ju. Email: jurong@mail.sysu.edu.cn
†The authors wish it to be known that, in their opinion, the first three authors should be regarded as Joint First Authors.

genomic deletion of RPs was observed in approximately 43% of TCGA tumor specimens (8), the association between tumors and RP expression levels is complicated and depends on the tumor type. For instance, the mRNA levels of *uL24*/*RPL26*-like (*RPL26L1*) and *eS27*/*RPS27*-like (*RPS27L*) are exclusively upregulated in breast and thyroid carcinomas, while the *eL21*/*RPL21* mRNA level is decreased in breast and uterine cancers (9). The heterogeneity of RPs in terms of expression and ribosomal composition implies the diversified functional relevance of RPs, consistent with accumulating evidence that emphasizes the involvement of RPs in specific cellular functions and phenotypes. For instance, mutations in certain RPs associated with Diamond-Blackfan anemia (DBA) selectively lead to bone marrow failure (10,11). Another example of the functional specification of RPs is *eL38*/*RPL38*, which is required for ribosome-mediated control of Hox mRNA translation during vertebrate tissue patterning (12,13).The functional heterogeneity of RPs could originate via distinct mechanisms, including specialized RP compositions with preferential translational control of mRNA subsets (7,14,15), altered ribosome concentrations (11,16), or the involvement of other extraribosomal cellular factors with certain RPs, such as *uL13*/*RPL13a* (17).

Despite these studies, a systematic understanding of the functional association of RP heterogeneity is still lacking. In the present study, we characterized genome-wide gene expression changes at the translational and transcriptional levels by ribosome profiling (Ribo-seq) and RNA sequencing (RNA-seq) after knocking down 75 individual human RP mRNAs. Our results revealed that RP deficiency induced divergent gene expression changes, particularly at the translational level. The other RPs were subjected to cotranslational regulation upon single RP repression, where deficiency of the large subunit (60S) or the small subunit (40S) had opposite effects on the remaining subunits. RP deficiency altered genes associated with eight major biological functions, including the cell cycle, cellular metabolism, signal transduction and development. Deficiency of 60S RPs displayed greater inhibitory impacts on cell growth than did depletion of 40S RP genes via P53 signaling. Regarding the functional preference conferred on cells lacking different RPs, we showed that *eS8*/*RPS8* deficiency stimulated cellular apoptosis while *eL13*/*RPL13* or *eL18*/*RPL18* deficiency promoted cellular senescence. We also validated specific phenotypic associations of *uL5*/*RPL11* and *eL15*/*RPL15* with retinal development and angiogenesis, respectively. Overall, our study demonstrates the widespread functional relevance of RPs in controlling specific cellular activities, providing new biological insights into ribosome regulation in development and diseases. In addition, it offers a comprehensive resource valuable to a broad community.

MATERIALS AND METHODS

Ribosomal protein naming system

Considering that RP gene names are not necessarily the same as the names of the corresponding ribosomal proteins and that the names of the RP genes encoding the same protein can indeed vary from organism to organism, in the present study, we used the RP gene names recommended by a previous study (18) (Supplementary Table S6).

Cell lines

A549 cells, U2OS cells, and Neuro-2a cells were obtained from the American Type Culture Collection (ATCC). A549 and U2OS cells were cultured in Dulbecco's modified Eagle's medium (DMEM) supplemented with 10% fetal bovine serum (FBS) (Gibco, 10270-106) and antibiotics (100 μg/ml penicillin and 50 μg/ml streptomycin sulfate) (Gibco, 15140122). Neuro-2a cells were maintained in modified Eagle's medium (MEM) supplemented with 10% FBS, antibiotics (100 μg/ml penicillin and 50 μg/ml streptomycin sulfate) and 1% NEAA (Gibco, 11140050). HUVECs were purchased from ScienCell Research Laboratories (ScienCell, 8000) and cultured in EGM-2 medium (Lonza, CC-3162). All cell lines were genotyped to confirm their identity at GENEWIZ. Cells were incubated at 37°C with 5% CO_2, and tested routinely for mycoplasma contamination.

siRNA transfection

A549 cells were transfected for 24 h with RP-targeting or nontargeting (control) siRNAs at a final concentration of 40 nM using Lipofectamine RNAiMAX reagent (Invitrogen, catalog no. 13778150) following the manufacturer's protocol.

Animals

All experiments on animals were performed according to the IACUC (Institutional Animal Care and Use Committee) standards, and approved by Zhongshan Ophthalmic Center, Sun Yat-sen University. CD1 mice were purchased from Vital River Laboratories (Beijing, China).

Quantitative real-time PCR (qRT–PCR)

Total RNA was isolated with TRIzol (Invitrogen, 15596018) following the manufacturer's protocol. cDNA was synthesized from 1 μg of total RNA using HiScript II Q RT SuperMix for qPCR (Vazyme, R223-01). Real-time PCR was performed using iTaq™ Universal SYBR Green Supermix (Bio-Rad, 1725121) in a CFX96 system (Bio-Rad). Each reaction was performed in triplicate. The primers are listed in Supplementary Table S7. The mRNA expression fold changes were calculated by the $\Delta\Delta Ct$ method using the housekeeping gene GAPDH or β-actin as the internal control with normalization to the experimental control.

Library preparation for RNA-seq and Ribo-seq

A549 cells were harvested 5 min after treatment with 100 μg/ml cycloheximide (CHX) (Sigma, C4859) in DMEM and washed twice in PBS containing 100 μg/ml CHX. Samples were lysed with 1 ml of mammalian lysis buffer containing 200 μl of 5× Mammalian Polysome Buffer (Epicenter, RPHMR12126), 100 μl of 10% Triton X-100, 10 μl of 100 mM DTT, 12.5 μl of Turbo DNase (Invitrogen, AM2239), 1 μl of 100 mg/ml CHX, and 675.5 μl

of nuclease-free water. After incubation for 20 min on ice, lysates were centrifuged at 12 000 rpm and 4°C for 10 min. For each sample, the lysate was divided into two aliquots (~600 μl for Ribo-seq and 150 μl for RNA-seq). For the 600-μl lysate aliquots, 6 units of ARTseq Nuclease were added to each A260 lysate, and the mixtures were incubated for 60 min at room temperature with rotation. Nuclease digestion was stopped by adding 10 μl of SUPERase·In RNase Inhibitor (Ambion, AM2696). Lysates were loaded onto MicroSpin S-400 HR spin columns (GE Healthcare, 27-5140-01). Total RNA was purified with a Zymo RNA Clean & Concentrator-25 Kit (Zymo Research). rRNA was depleted with a Ribo-Zero Gold rRNA Removal Kit (Illumina, MRZG126). The rRNA-depleted samples were separated on a 10% TBE–urea polyacrylamide gel. Ribosome-protected fragments with lengths between 28 nt and 30 nt were selected. Ribo-seq libraries were then constructed following a protocol described previously (19). For the 150-μl lysate aliquots, total RNA was isolated with a Zymo RNA Clean & Concentrator-25 Kit (Zymo Research) and RNA-seq libraries were constructed with a VAHTS Total RNA-seq (H/M/R) Library Prep Kit (Vazyme, NR603-02) according to the manufacturer's instructions. All libraries were subjected to PE150 sequencing in an Illumina HiSeq X10 or a NovaSeq 6000 system.

Cell cycle analysis

Approximately 1.2×10^5 cells were seeded in 6-well plates and transfected with siRNA on the following day at ~40% confluence. Cells in exponential growth phase were collected 24 h after siRNA transfection and fixed with 100% methanol at −20°C overnight. Fixed cells were washed twice with PBS and treated at 37°C for 30 min with staining buffer containing 25 μg/ml propidium iodide (Sigma, P4864) and 50μg/ml RNase A (Invitrogen, EN0531). The DNA content was measured by flow cytometry (BD, LSR Fortessa) and analyzed by ModFIT software (v4.1).

Western blotting

Cell lysates were collected 24 h after RP knockdown, denatured at 100 °C for 5 min and separated on 12% PAGE gels (30 min at 70 V followed by 1 h at 100 V). The extracted proteins were electroblotted onto polyvinylidene fluoride (PVDF) membranes (Millipore). Membranes were blocked with 5% nonfat dry milk in TBST for 1 h and incubated with the following primary antibodies: 1:1000 dilution of anti-p53 (CST, 2524s), 1:2000 dilution of anti-p21 (CST, 2947s), 1:5000 dilution of anti-GAPDH (Proteintech, 60004), anti-eS8/RPS8 rabbit polyclonal (Proteintech,18228), anti-uL5/RPL11 polyclonal (Proteintech,16277), anti-eL13/RPL13 rabbit polyclonal (Proteintech,16241), anti-eL15/RPL15 rabbit polyclonal (Proteintech,16740), anti-eL18/RPL18 rabbit polyclonal (Affinity Biosciences, DF3700), anti-eL22/RPL22 (Novus Biologicals, NBP1-06069), anti-eL29/RPL29 polyclonal (Proteintech, 15799), anti-Sox9 (Millipore, AB5535) and anti-FOXO1 (C29H4) rabbit mAb (CST, 2880). Membranes were then incubated with horseradish peroxidase-conjugated anti-mouse or anti-rabbit secondary antibodies at a 1:10 000 dilution for 2 h. Immunoreaction signals were visualized with Immobilon Western Chemiluminescent HRP Substrate (Millipore) and imaged with a Chemi-Doc™ Imaging System (Bio-Rad).

Cell proliferation and apoptosis analyses

A549 cells transfected with siRNAs were seeded (~0.6×10^5 cells/well) and grown in 24-well plates for 0, 24, 48 and 72 h. Cell proliferation was assessed by adding 100 μl of 5 mg/ml 3-[4,5-dimethylthiazol-2-yl]-2,5-diphenyltetrazolium bromide (MTT) for 4 h at 37°C, prior to aspiration of the medium and the addition of 300 μl of dimethyl sulfoxide. Each reaction was performed in triplicate. Spectrophotometric measurements at 490 nm were obtained with a Synergy H1 microplate reader (Bio Tek). Apoptosis was measured by a TUNEL assay. Dead cells were detected by DNA fragmentation using *In Situ* Cell Death fluorescein (Roche, 11684795910) following the manufacturer's instructions.

Cell senescence detection

A549 cells were seeded in 6-well plates, transfected with siRNA on the following day at ~30% confluence, trypsinized and counted in triplicate 72 h after transfection. Senescence-associated-β-galactosidase (SA-β-gal) activity was assayed according to the manufacturer's instructions (CST, 9860).

Preparation of conditioned medium (CM) from *RPL15*-deficient A549 cells

A549 cells were seeded in 12-well plates at a density of 1×10^5 cells/well in DMEM and transfected with *RPL15*-targeting or control siRNAs using Lipofectamine RNAiMAX reagent according to the manufacturer's protocol. The medium was replaced with EBM2 containing 0.5% FBS at 6 h. For normoxic culture, cells were cultured in a CO_2 incubator for 18 h. For hypoxic culture, cells were cultured in a modular incubator chamber that was flushed with 1% O_2/5% CO_2/balance N_2 at 37°C for 18 h; CMs were harvested, centrifuged at 1000 rpm for 10 min, and stored at −20°C.

ELISA for VEGF

VEGF concentrations in the CMs from *RPL15*-deficient and control A549 cells cultured under normoxic or hypoxic conditions were determined with a Human VEGF Valukine ELISA Kit (Novus, val106).

Wound healing assay

HUVECs were seeded in 6-well plates at a density of 2×10^5 cells per well and incubated until an even monolayer at ~90% confluence had formed. The HUVEC monolayers were scraped with a 200-μl pipet tip. The wells were washed with PBS to remove detached cells before incubation with CMs. The healing wounds were photographed at 0 and 8 h.

Tube formation assay

The wells of 48-well plate were coated with growth factor-reduced Matrigel (Corning, 354230) and incubated at 37°C for 30 min to allow the matrix solution to polymerize. HUVECs were seeded on the gel and cultured in CM for 48 h at 37°C with 5% CO_2. To assess tube formation and disassembly, cells were photographed at 6, 12, 18, 24, 30 and 48 h. Tube numbers and lengths were evaluated by ImageJ software (20). Each experiment was repeated six times.

shRNA plasmids and RNAi interference of RPs in mouse retinas

In vivo conditional knockdown of *uL5/Rpl11* or *eL29/Rpl29* in the retina was performed in neonatal mice. For knockdown experiments, selected short hairpin RNA sequences were inserted into the shRNA interference vector pBS/U6 containing the human U6 promoter (21). The primer sequences used for construction of the pBS/U6-shRNA plasmids are listed in Supplementary Table S1. The knockdown efficiency was assessed by qRT-PCR in neuro-2a cells. The constructs with high knockdown efficiency were used in the following experiments. The targeting sequence for mouse *Rpl11 (uL5/Rpl11)* was 5′-CCGCAAGCTCTGCCTCAATAT-3′ (*uL5/Rpl11*-sh), the targeting sequence for *eL29/Rpl29* was 5′-GCCAAGAAGCACAACAAGAAA-3′ (*eL19/Rpl29*-sh), and the non-targeting shRNA control (shNT) sequence was 5′-GCGCGATAGCGCTAATAATTT-3′. To perform retinal knockdown, the pBS/U6 constructs and the pCIG vector (as a GFP reporter) were mixed at a ratio of 2:1 (μg/μl). A 1 μl volume of the mixture was injected into the subretinal space of P0 CD1 mice with a microliter syringe (Hamilton). Immediately following injection, electric pulses (100 V; five 50-ms pulses at 950-ms intervals) were applied with the '+' electrode of tweezer-style electrodes (BTX) positioned on the injected eye. Transfected retinas were collected on P12 for analysis when the large majority of retinal cells were committed and developed into mature cell types.

Polysome profiling

Polysome profiling was conducted following the protocol described in a previous study (22). In detail, one 10 cm dish of A549 cells was treated with 100 μg/ml CHX in DMEM at 37°C for 5 min prior to harvesting, and the cells were then washed twice with cold PBS containing 100 μg/ml CHX. Samples were lysed with 800 μl of lysis buffer containing 10 mM Tris–HCl (pH 7.4), 5 mM $MgCl_2$, 100 mM KCl, 1% Triton X-100, 2 mM DTT, 100 μg/ml CHX, Complete Protease Inhibitor EDTA-free (Roche, 4693132001) and 20 U/mL SUPERase-In RNase Inhibitor and were then harvested by scraping, transferred to Eppendorf tubes, and incubated on ice for 10 min. Lysates were centrifuged at 10 000 × g for 10 min at 4°C. RNA concentrations were measured with a Nanodrop UV spectrophotometer (Thermo Fisher Scientific). Equal amounts of lysates were layered onto a linear sucrose gradient (10–50%, w/v) with gradient buffer containing 20 mM HEPES–KOH (pH 7.4), 5 mM $MgCl_2$, 100 mM KCl, 2 mM DTT, 100 μg/ml CHX, and 20 U/ml SUPERase-In RNase Inhibitor, and were then centrifuged in an SW41 Ti rotor (Beckman) for 2 h at 36 000 rpm at 4°C. Samples were fractionated and analyzed with a Gradient Station (BioComp).

Construction and screening of a lentiviral sgRNA library for human RPs

sgRNA sequences (Supplementary Table S8) for human RP genes were retrieved from the Brunello library (23). Four sgRNAs for each RP and 80 nontargeting sgRNAs were designed and synthesized with a CustomArray 12K array chip (CustomArray, Inc.). A plasmid library was constructed following the protocol described in a previous study (23) with minor modifications. sgRNA libraries were amplified as subpools by nested PCR. For the first round of PCR, all sgRNAs were amplified using Phusion Flash High-Fidelity PCR Master Mix (NEB, M0531L) with the following primers: sense, 5′-ACGCTCAGTTCATATCATCACG-3′ and antisense, 5′-ATCGCAGCATCTACATCCGATGT-3′. A second round of PCR was performed to incorporate overhangs compatible with the lentiCRISPRv2 vector using the following primers: sense, 5′-TTTCTTGGCTTTATATATCTTGTGGAAAGGACGAAACACCG-3′ and antisense, 5′-GACTAGCCTTATTTTAACTTGCTATTTCTAGCTCTAAAAC-3′.

Meanwhile, the lentiCRISPRv2 plasmid was digested using *BsmB*I and purified. The digested plasmids and sgRNAs were ligated using Gibson Assembly Master Mix and transformed into competent DH5α cells. The average number of clones for each sgRNA was approximately 400.

Lentivirus were produced by cotransfection of lentiCRISPRv2-sgRNA-RPs with pVSVg and psPAX2 into 293T cells using Lipofectamine 3000 reagent (Invitrogen, L3000). The medium was changed 6 h after transfection. The virus-containing supernatant was collected 48 h after transfection and filtered through a 0.45 μm filter. A549 cells were infected with sgRNA library lentiviruses at an MOI of < 0.3. Genomic DNA extraction was conducted on two batches of cells: the first batch of cells (5×10^6) was collected 2 days after infection using a TIANamp Genomic DNA Kit (Tiangen, DP304), and the second batch of cells treated with puromycin was collected at 7 d. For each library, first, the lentiviral integrated sgRNA-coding regions were PCR-amplified using the sense primer 5′-AATGGACTATCATATGCTTACCGTAACTTGAAAGTATTTCG-3′ and the antisense primer 5′-TCTACTATTCTTTCCCCTGCACTGTtgtgggcgatgtgcgctctg-3′ with TransTaq HiFi DNA polymerase, and the sequencing libraries were then amplified with Titanium Taq (Clontech, 639209) with the following barcoded primers.

Control sample: sense, 5′-AATGATACGGCGACCACCGAGATCTACACTCTTTCCCTACACGACGCTCTTCCGATCTtAAGTAGAGtcttgtggaaaggacgaaacaccg-3′, and antisense, 5′- AAGCAGAAGACGGCATACGAGATAAGTAGAGGTGACTGGAGTTCAGACGTGTGCTCTTCCGATCTtTCTACTATTCTTTCCCCTGCACTGT-3′.

Experimental samples: sense, 5′-AATGATACGGCGACCACCGAGATCTACACTCTTTCCCTACACGACGCTCTTCCGATCTatACACGA

TCtcttgtggaaaggacgaaacaccg-3′, and antisense, 5′-CAAGCAGAAGACGGCATACGAGATACACGA TCGTGACTGGAGTTCAGACGTGTGCTCTTCCG ATCTatTCTACTATTCTTTCCCCTGCACTGT-3′. The products were further purified with a gel extraction kit (Tiangen, DP209) and prepared for sequencing on the Illumina Novaseq 6000 system.

Quantification and assessment of sgRNA effects in CRISPR experiments

Sequencing reads containing specific sgRNA sequences were grouped and counted. The sum of all the counted reads for each library was considered the library size. The normalized sgRNA expression levels were calculated by dividing the sgRNA counts by the corresponding library size. The minimal ratio of the sgRNA expression level on Day 7 to that on Day 2 was defined as the cell growth inhibitory effect of knockdown of the corresponding RP. For quality control, normalized sgRNA expression levels on Day 7 and Day 2 were compared. Theoretically, the expression levels of the nontargeting sgRNAs would be increased on Day 7 while those of the RP-targeting sgRNAs would be decreased on Day 7. The inhibitory effect for each RP in our assays correlated (PCC; $R = 0.46$, $P = 3.8e{-}05$) with that in the Cancer Dependency Map Project (DepMap) database (https://depmap.org/portal/) (24).

Sequencing data processing and quality control for RNA-seq and Ribo-seq

Base calls were demultiplexed and converted to fastq files with Bcl2fastq (v2.20.0.422) (https://support.illumina.com/downloads/bcl2fastq-conversion-software-v2-20.html). Adapters and low-quality reads ending with quality scores <20 were trimmed by Cutadapt (v1.8.1) (http://code.google.com/p/cutadapt/). Trimmed reads with a length <20 nt were discarded. Reads aligned to human rRNA and tRNA sequences extracted from the UCSC Genome Browser (http://genome.ucsc.edu/) (25) were further excluded. For Ribo-seq libraries, trimmed reads with a length <26 nt or >34 nt were excluded. The remaining reads were aligned to the human genome (Ensembl GRCh38.88) (26) with STAR (v2.6.1-d) (https://github.com/alexdobin/STAR) (27).

For quality control, we assessed multiple aspects of each library. (a) Total and unique alignments were summarized by STAR using the resulting files. (b) Gene body coverage was estimated to test whether sequence bias occurred in the 3′ or 5′ end of transcripts with the '*geneBody_coverage.py*' function in RSeQC (28). (c) Relative percentages of alignments to gene features (CDS, 5′ UTR and 3′ UTR of annotated transcripts according to the GTF file) were estimated with the '*read_distribution.py*' function in RSeQC. For gene body coverage and read distribution analyses, we included transcripts that had a combined exon length >1000 nt and contained at least two exons. (d) For Ribo-seq libraries, frame distributions and ribosomal footprints around the start or stop codons were analyzed with the '*ribotish quality*' function with default parameters, embedded in Ribo-TISH (v0.2.2) (29).

Gene expression quantification, normalization and differential analyses

To allow for proper comparison and integration of mRNA-seq and Ribo-seq data, all RNA-seq quantifications were derived from the first reads mapped to the defined genomic features in the Ensembl GTF file, as described in a previous study (30). Unique alignments to exons in RNA-seq data and to CDSs in Ribo-seq data were counted with featureCounts (v1.6.0) (31) for quantification of gene expression. Raw gene counts were converted to RPKM (reads per kilobase per million mapped reads) values with the following equation:

$$\mathrm{RPKM} = \frac{\text{gene count} \times 10^9}{\text{Total number of mapped reads} \times \text{gene length in nt}}.$$

For the RNA-seq and Ribo-seq datasets, we included the genes with a mean RPKM > 1 across all libraries in further analysis ($n = 13\,294$ for RNA-seq; $n = 11\,694$ for Ribo-seq). We set up replicates for 16 RPs and the replicates showed high reproducibility; thus, we combined the replicates using the mean RPKM values to define gene expression. Our sequencing data included hundreds of libraries, prepared in several batches. Batch effects in RNA-seq and Ribo-seq data were evaluated and eliminated with ComBat (32) in the 'sva' package (33). Differential expression analysis was performed by comparing normalized gene expression in RP-deficient cells with that in control cells from the same batch. For both RNA-seq and Ribo-seq data, we defined differential genes as those with an expression fold change of ≤ 0.5 or ≥ 2.

Reproducibility analysis

To test the reproducibility of our experiments, we conducted Pearson correlation analysis to compare genome-wide gene expression levels between replicates in our experiments and between our control cells and A549 cells in public RNA-seq and Ribo-seq datasets, which were downloaded from the Cancer Cell Line Encyclopedia (CCLE) database and the GEO datasets under accession number GSE82232 (34), respectively. In practice, the averaged expression level for each gene across all replicates were compared between our data and external datasets. Moreover, we compared the functional associations in our analysis with those in previous studies by an extensive literature search.

Cluster analysis of differential genes

The differential genes for each RP were combined and clustered to detect common or distinct signals corresponding to downstream gene expression changes between RPs. In detail, indicator matrices containing the values –1, 0 and 1 for RNA-seq and Ribo-seq data, where each row represents a gene and each column represents a specific RP, were used. In the indicator matrices, a value of 1 refers to genes upregulated, –1 refers to genes downregulated, and 0 refers to genes with unchanged expression after knockdown of the indicated RP. For RP clustering, the *hclust* function was used with the RP correlation matrix as input. For gene clustering,

kmeans was used. Cluster visualization was performed using the 'Heatmap' function in the ComplexHeatmap package (35).

Functional enrichment analyses

For each RP, GO enrichment (36) and KEGG pathway (37,38) analyses were conducted with the gprofiler2 package, an interface for the g:Profiler toolset (https://biit.cs.ut.ee/gprofiler/gost) (39). The upregulated and downregulated genes were used as input for each RP. To remove the redundancy between GO terms, the *hclust* function was used according to the similarity measurement performed with the 'GOSemSim' package (40,41) and GO categories were determined by the 'silhouette' method.

Translational efficiency estimation and differential analysis

Translational efficiency (TE) estimation was performed by calculating the ratio of the gene expression level from Ribo-seq data to that from RNA-seq data. In detail, for the RNA-seq and Ribo-seq libraries, we only counted the unique alignments that were fully contained within the CDS, thus avoiding counting reads that overlapped multiple features. Raw gene counts were then converted to RPKM values. Batch effects were also assessed and excluded. Normalized gene expression matrices for the RNA-seq and Ribo-seq data were then used to calculate the TE. Differential analysis was performed by comparing the TE in RP-deficient cells with that in the control cells from the same batch.

Separating transcriptional and translational regulation

RPFs in Ribo-seq data reflect the combined outcome of transcriptional and translational control of gene expression. A gene's regulation mode was defined by intersecting the changes identified by RNA-seq (DEGs), Ribo-seq (DTGs) and TE assessment (DTE). In total, four classes of regulation modes were defined-forwarded, exclusive, intensified and buffered regulation, where forwarded regulation indicated that the changes identified by Ribo-seq were explained by the changes identified by RNA-seq, exclusive regulation indicated that the changes in TE occurred exclusively without underlying changes in mRNA expression, buffered and intensified regulation indicated that both the TE and mRNA expression were chagned.

Other datasets

Quantitative data for P53 protein levels and the impact on nucleolar disruption, which was estimated by quantification of nuclear stress (iNO index) after RP deficiency, were extracted from Emilien Nicolas *et al.*'s study (42). In brief, these researchers used specific siRNAs to deplete individual RPs in FIB364 or HCT116 cells. A549 cell RNA-seq data was extracted from CCLE with the 'depmap' package.

Defining cell type-specific genes in A549 cells

To identify the cell type-specific expressed genes in human cancer cell lines, quantitative RNA-seq-based gene expression data for 1165 cancer cell lines was extracted with the 'depmap' package, a tool for the CCLE database (43). Aggregated log2 transformed TPM values were used. We defined the genes with TPM values > the mean + 2SD as cell type-specific genes for a certain cell type. We identified a total of 478 mRNAs with A549 cell-specific expression, of which 199 were protein-coding genes. We focused on the protein-coding genes in our further analyses. Fisher's exact test was used to check whether the differentially expressed genes for each RP were enriched with A549 cell-specific expressed protein-coding genes.

Extraction and characteristics of transcript features

Nucleotide sequences for genome-wide or individual transcript features, such as the 5′ UTR, were extracted from the Ensembl database (26). Transcripts with short 5′ UTRs (<20 nt) or long 5′ UTRs (>500 nt) (11) were excluded from further analysis. To quantify mRNA structural complexity, the minimum free energy (MFE) was predicted for selected transcripts with RNAfold (https://www.tbi.univie.ac.at/RNA/RNAfold.1.html) (44). The GC content and length of mRNAs of interest were estimated with the 'seqinR' package (http://r-forge.r-project.org/projects/seqinr/) (45). The Kozak sequence was defined using the sequence beginning 10 nt upstream of the start codon for each transcript. Kozak sequence similarity analysis and visualization were performed with the 'motifStack' (46) and 'ggseqlogo' (47) packages, respectively.

Quantification and statistical analysis

Statistical information, including n, mean, and statistical significance values, is indicated in the text or the figure legends. Data were statistically analyzed using Student's t test or analysis of variance (ANOVA) with multiple comparisons, as appropriate, using Prism 8.0 (GraphPad Software, Inc). A P value of <0.05 was considered to be statistically significant.

RESULTS

Overview of the transcriptome and translatome analysis results

To achieve a systematic understanding of the molecular and functional relevance of human RPs, we knocked down each of the 78 RPs using specific siRNAs in A549 cells and then performed parallel RNA-seq and Ribo-seq analyses. Twenty-four hours after siRNA transfection, cells were harvested, and RNA was extracted for library preparation and HT sequencing (see Methods). At least two siRNAs for each RP gene were designed to avoid off-targeting (Supplementary Table S1). The siRNA knockdown efficiencies were validated via RT-qPCR. As summarized in Supplementary Figure S1A and Supplementary Table S2, the residual mRNA levels of the RPs after siRNA knockdown were only a small fraction of the corresponding levels in the control cells, with a median of 2% across all the RP targets, suggesting that the siRNAs achieved high knockdown efficiency. We prepared 105 paired RNA-seq and Ribo-seq libraries for the 78 RPs, together with 8 control samples treated with

nontargeting siRNAs, and biological replicates were performed for 16 RPs and 3 control samples. The Ribo-seq and RNA-seq datasets of 75 RPs passed stringent quality control criteria and were retained for further analyses (see Methods) (42). In total, the Ribo-seq and RNA-seq analyses yielded approximately 14 and 3.6 billion clean reads aligned to the human reference genome, respectively, with corresponding averages of approximately 33 and 32 million uniquely mapped reads per library (Supplementary Table S3).

For each library, ribosome-protected fragments (RPF) in the Ribo-seq data showed the expected size distributions, mainly ranging from 28 to 32 nucleotides (nt) (Figure 1A). While the RNA-seq libraries were evenly mapped to transcripts along the 5′ to 3′ orientation, the Ribo-seq alignments presented characteristic 5′ ramps, with ribosome footprints decreasing along the gene body (Supplementary Figure S1B) (48). Both the Ribo-seq and RNA-seq reads showed significantly higher density in coding sequences (CDSs) (*t* test, all $P < 2.2e{-}16$) (Supplementary Figure S1C, D). The relative percentages of the Ribo-seq reads distributed in the CDS, 5′ untranslated region (UTR) and 3′ UTR were 97.7%, 2.1% and 0.2%, respectively, showing strong preference for the CDS and depletion in the 3′ UTR relative to the RNA-seq reads (87.6% in the CDS, 1.0% in the 5′ UTR and 11.4% in the 3′ UTR) (Figure 1B, C), consistent with the typical read distribution across genomic regions for Ribo-seq and RNA-seq (49). As expected, Ribo-seq alignments to the CDS showed clear 3-nucleotide periodicity, with ∼58% of the reads in the first reading frame on average (Figure 1D-F). In contrast, the RNA-seq reads showed no frame preference (Supplementary Figure S1E). The Pearson correlation coefficients (PCCs) of the biological replicates ranged from 0.9760 to 0.9962 for the Ribo-seq (median, 0.9936) and from 0.9576 to 0.9929 for the RNA-seq (median, 0.9884) analyses, suggesting the high reproducibility of our experiments (Figures 1G; Supplementary Figure S1F, G). Our A549 control cells also showed a high degree of gene expression similarity compared to that in public A549 cell datasets (see Methods), with PCCs of 0.81 and 0.83 for the Ribo-seq and RNA-seq analyses, respectively (Supplementary Figure S1H). Taken together, these results suggested that our data were of high-quality and highly reproduceable.

Landscape of gene expression changes

In comparing RP-deficient cells with control cells, we identified 9264 differentially translated genes (DTGs) by Ribo-seq and 6743 differentially expressed genes (DEGs) by RNA-seq for 75 RPs (see Materials and Methods). Deficiency of each RP impacted a distinct subset of genes at both the transcriptional and translational levels (Supplementary Figure S2A, B), where the DTG numbers ranged from 317 to 2631, with a median of 1299, and the DEG numbers ranged from 97 to 1676, with a median of 476 (Figure 2A). In addition, 73% of the DEGs and 51% of the DTGs were shared by no more than five RPs, while only 7.6% of the DEGs and 18.36% of the DTGs were shared by more than 20 RPs, a pattern following a power-law distribution (Figure 2B). We observed significantly more DTGs than DEGs for 72 RPs (Wilcoxon test, $P < 2.2e{-}16$; Figure 2C, Supplementary Figure S2C) and larger-magnitude changes for the DTGs than for the DEGs, as determined by the differences in the 97.5% and 2.5% quantiles of the fold change values (Wilcoxon test, $P < 2.2e{-}16$; Figure 2D). These results indicated that RP deficiency caused more drastic changes at the translational level than at the transcriptional level.

Comparison of the DEGs and DTGs for each RP showed that the percentage of overlapping genes, as quantified by the Jaccard index, ranged from 2.72% to 46.50%, with a median of 20.90%, indicating that RP deficiency induced a large degree of uncoupled gene expression changes both transcriptionally and translationally. We next accounted for the transcriptional and translational contributions to these gene expression changes. The differential genes identified by RNA-seq and Ribo-seq for each RP were categorized into four regulatory modes—intensified, buffered, exclusive, and forwarded—based on their changes in terms of RPF reads, mRNA reads and translational efficiency (TE) (Supplementary Figure S2D). Specifically, forwarded genes had RPF changes that were explained by mRNA expression changes. Exclusive genes had changes in the TE without mRNA expression changes. Buffered and intensified genes had changes in the TE that offset or amplified, respectively, the changes in mRNA expression. Of the 75 RPs, 66 could be categorized into one or two major regulation modes (Figure 2E). Deficiency of most RPs (35) induced exclusive regulation, while 13 showed dominant forwarded regulation. In addition, 13 RPs showed both exclusive and forwarded regulation. These results indicated that deficiency of individual RPs mainly affected gene expression at the translational level, probably via a ribosome-mediated process. Further functional analysis showed that the affected genes with the same regulation mode for different RPs were enriched in different functions (Supplementary Figures S2E-K). For example, genes downregulated under translational exclusive regulation of *RPS12* deficiency were related to the transferase activity function, while those downregulated under translational exclusive regulation of *RPS26* deficiency were related to the aminoglycan metabolic process (Supplementary Figure S2E).

Coregulation of 60S and 40S RPs after RP deficiency

Previous studies showed that deficiency of individual RPs can result in dysregulation of other RPs, further leading to an imbalance in stability and the accumulation of ribosomal subunits (50,51). Our dataset offers the opportunity for a systematic investigation of RP coregulation upon RP disruption in human cells, especially at the translational level. Substantial downregulation of each RP targeted by specific siRNAs was observed at both the transcriptional and translational levels (the diagonal line in Figure 3A and Supplementary Figure S3A), confirming the high knockdown efficiencies of siRNA transfection in our samples. A distinct pattern was observed at the translational level, where knocking down 60S RPs suppressed the expression of RPs of both subunits, while knocking down 40S RPs resulted in elevated expression of RPs of both subunits. However, at the transcriptional level, knocking down RPs had smaller

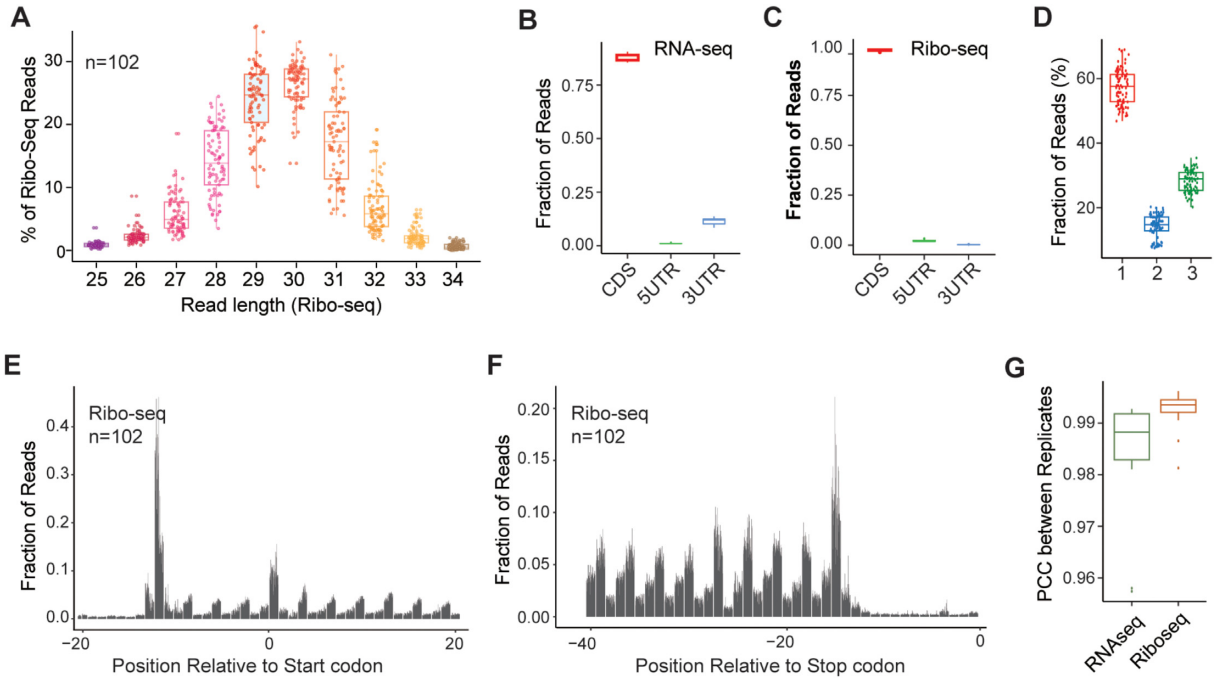

Figure 1. Overview of the transcriptome and translatome datasets. (**A**) Length of RPFs in Ribo-seq libraries for all samples. Each point indicates one library. (**B**, **C**) The relative fraction of reads mapped to the CDS, 5′ UTR and 3′ UTR of annotated transcripts in RNA-seq (B) and Ribo-seq (C) libraries. When genome features were overlapped, CDS exons were prioritized over UTR exons. (**D**) Percentages of RPFs mapped to reading frames by combining all Ribo-seq libraries. Each point indicates one library. (**E**, **F**) Fractions of reads assigned to each nucleotide around the start codons (E) or stop codons (F) for all libraries in Ribo-seq data. Each bar indicates one sample. P-site was used to assign the short read to transcript location. (**G**) Pearson correlation coefficients between replicates in RNA-seq and Ribo-seq datasets. Log_2 RPKM values were used in the correlation analysis.

effects on the changes in the expression of the untargeted RPs (t test, $P = 4.41e{-}15$; Supplementary Figure S3B). Interestingly, we also observed opposite effects of modulation of RPs from the 60S and the 40S subunits, where knocking down 60S RPs slightly increased the levels of mRNAs encoding proteins of both subunits, while knocking down 40S RPs slightly decreased the levels of mRNAs encoding proteins of both subunits (Supplementary Figure S3A). TE-based analyses showed that knocking down 60S RPs led to a global decrease in the TE, whereas knocking down 40S RPs resulted in a global increase in the TE of RPs (Figure 3B).

Because RPs enter the assembly pathway at different time points, and ribosome assembly begins in the nucleus, particularly in the nucleolus, and continues in the cytoplasm (2), we suspected that knockdown of the RPs that enter the assembly pathway earlier might have a larger impact on RP translation than knockdown of the other RPs. To test this hypothesis, we annotated the RPs based on the cellular compartment at which they are assembled, that is, the nucleolus, nucleus, and cytoplasm (Figure 3C). We found that knocking down 60S RPs assembled in the nucleus reduced the expression of RPs at the translational level and their TE level to a greater extent than did knocking down those assembled in the cytoplasm (Wilcoxon test for RPF: nucleolus vs. nucleus, $P = 0.7339$; nucleolus vs. cytoplasm, $P = 0.0015$; nucleus vs. cytoplasm, $P = 0.0225$; Wilcoxon test for TE: nucleolus vs. nucleus, $P = 0.4134$; nucleolus vs. cytoplasm, $P = 0.0225$; nucleus vs. cytoplasm, $P = 0.0002$; Figure 3D), suggesting that deficiency of 60S RPs entering the assembly pathway in the nucleus, including the nucleolus, had a greater effect on the translational repression of RPs than did deficiency of those entering in the cytoplasm. In contrast, we found no such assembly stage-dependent regulatory pattern upon knockdown of 40S RPs (Wilcoxon test for RPF: nucleolus versus nucleus, $P = 0.0675$; nucleolus versus cytoplasm, $P = 0.5663$; nucleus versus cytoplasm, $P = 0.2677$; Wilcoxon test for TE: nucleolus versus nucleus, $P = 0.9385$; nucleolus versus cytoplasm, $P = 0.1734$; nucleus versus cytoplasm, $P = 0.1061$).

We further investigated the impact of deficiency of 60S or 40S RPs on ribosome assembly. Polysome profiling by sucrose gradient-based centrifugation can be used to assess the relative abundances of free 40S and 60S subunits by quantifying the corresponding peaks in the profile. Polysome profiles of four RP genes, two encoding 60S RPs (*uL5/RPL11* and *eL15/RPL15*) and two encoding 40S RPs (*eS8/RPS8* and *eS25/RPS25*), were analyzed (Figure 3E). We observed that knockdown of *uL5/RPL11* or *eL15/RPL15* decreased free 60S and increased that of 40S, while knockdown of *eS8/RPS8* or *eS25/RPS25* increased free 60S and decreased that of 40S, which was consistent with the previous studies on defects of 60S RPs (52) and 40S RPs (50). Together, the results of our analysis demonstrated that deficiency of 40S and 60S RPs had opposite effects on the 60S and 40S subunits at the transcriptional and translational levels, as well as at the subunit assembly stage.

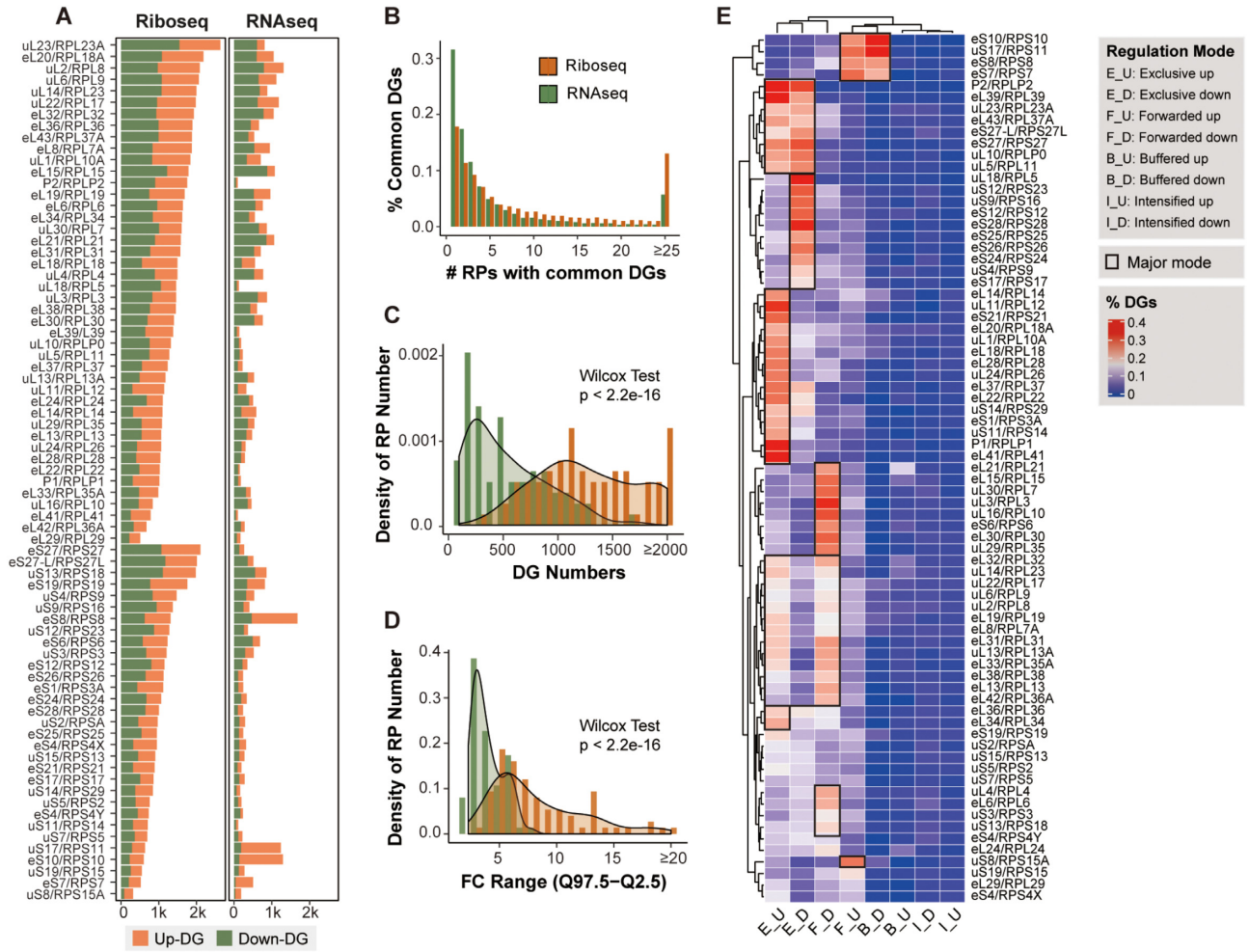

Figure 2. Diversity of gene expression changes upon RP knockdown. (**A**) Numbers of up- and down-regulated differential genes in RNA-seq and Ribo-seq for all RPs. RPs are ranked by DTG numbers in Ribo-seq. (**B**) Frequency of common DEGs or DTGs between RPs in RNA-seq and Ribo-seq. (**C**) Distribution of DEG or DTG numbers for all the RPs. The distributions in RNA-seq and Ribo-seq were compared by Wilcoxon sign-rank tests. (**D**) Ranges of global gene fold changes for all RPs. The ranges in RNA-seq and Ribo-seq were compared by Wilcoxon sign-rank tests. (**E**) Percentages of genes under different gene expression regulation modes after knockdown of each RP. RPs were grouped by hierarchical clustering analysis of the regulation profiles. Rectangles indicates the primary regulation mode for RP groups.

Functional characterization of the molecular landscape of RP-deficient cells

We next analyzed the functional relevance of the changed genes after knockdown of specific RPs. Individual knockdown of 64 RPs resulted in significant enrichment of gene ontology (GO) terms, grouped into eight major categories, including cell cycle, organelle organization, nucleotide and other macromolecular metabolism, signal transduction, cell response, cell and tissue development, and transport (Figure 4A, Supplementary Table S4; see Materials and Methods). We observed good agreement in the preferential functional impacts on the cell cycle and neurogenesis between A459 cells and HCT116 cells lacking *uL5/RPL11*, *eS6/RPS6* or *eS8/RPS8* (Supplementary Figures S4A-C). After an extensive literature search, we found that many known functional associations of RPs were reproduced in our study, for example, *eS6/RPS6* and *eL15/RPL15* in the cell cycle, *uL22/RPL17* in sex differentiation, *eS6/RPS6* in immune system development and *eL15/RPL15* in DBA (Figure 4B, Supplementary Table S5). These collective results again indicated that our analysis reliably reflected the functional relevance of RPs.

Based on the GO enrichment analysis results, the RPs were categorized into three groups. Deficiency of Group 1 RPs (31) usually impacted a large number of functional terms (median, 335), indicating the extensive functional associations of these RPs, while deficiency of Group 2 RPs (33) affected genes enriched in a small number of GO terms (median, 13), indicating preferential cellular functions (Figure 4A). In addition, deficiency of Group 3 RPs (11) resulted in changes in a small number of genes with no functional preference. Notably, Group1 was significantly enriched with 60S RPs (26 of 31 RPs; Fisher's exact test, $P = 0.0234$), suggesting that deficiency of 60S RPs generally had a larger impact on cellular functions than deficiency of 40S RPs. This was consistent with a previous study showing that knockdown of 60S RPs induced more severe nuclear disruption than knockdown of 40S RPs (42). Although de-

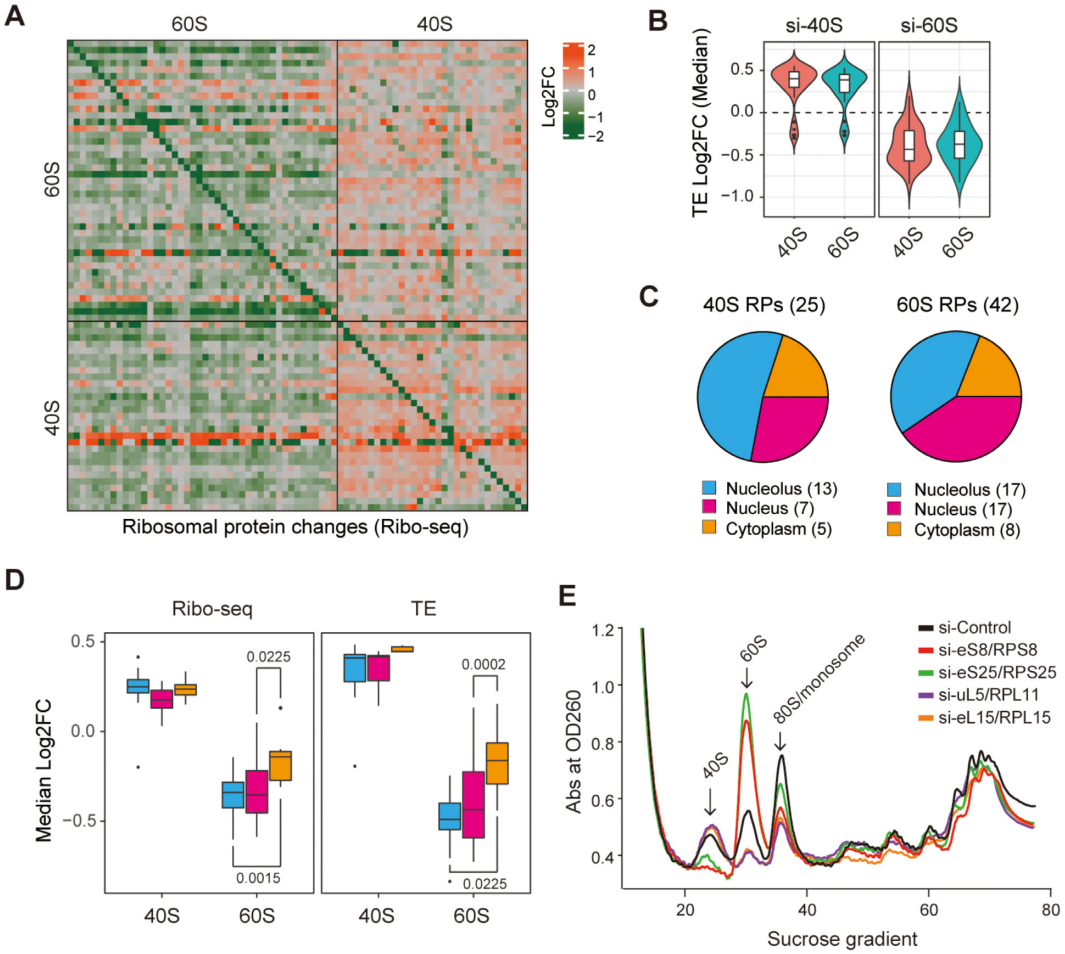

Figure 3. Co-regulation of 60S and 40S RPs. (**A**) The expression changes of RPs (rows) after knockdown of individual RPs (columns) in Ribo-seq dataset. Log_2 fold change values are shown. RPs for rows and columns according to ribosomal subunits as indicated by colored sidebars: cyan color indicates 60S RPs, orange color indicates 40S RPs. (**B**) Comparison of global changes in TE of 40S and 60S RPs after knockdown of RPs from 40S (left) or 60S (right). Median TE values of the remaining RPs were used for each RP targeted by siRNAs. (**C**) Numbers of RPs annotated to cellular locations where ribosomal assembly occurs. (**D**) Comparison of expression changes at the translatome level (left) and TE changes (right) of the remaining RPs after knockdown of individual RPs within different stages of ribosomal subunit assembly. Wilcoxon tests were performed to compare the difference between groups for each subunit. (**E**) Polysome profiling by sucrose-gradient-based centrifugation showing the changes in abundance of ribosomal components (40S, 60S, 80S monosome and polysomes) in A549 cells treated by specific siRNAs targeting *eS8/RPS8*, *eS25/RPS25*, *uL5/RPL11* or *eL15/RPL15*.

ficiency of 60S and 40S RPs resulted in similar numbers of DEGs (*t* test, $P = 0.10$), 60S RP deficiency led to significantly more DTGs than 40S RP deficiency (*t* test, $P = 0.018$; Supplementary Figure S4D). Moreover, 60S RP deficiency usually caused a greater magnitude of change in DEGs and DTGs (*t* test, $P < 0.05$; Supplementary Figure S4D). As expected, knocking down RPs from the same subunit resulted in more shared DEGs or DTGs than knocking down RPs from different subunits (Wilcoxon test, $P < 0.05$; Figure 4C), suggesting that a lack of RPs from the same subunit tends to alter the expression of similar genes.

Notably, all the RPs in Group 1 induced changes in the p53 signaling and cell cycle pathways upon knockdown. Consistent with this result, deficiency of these RPs increased the P53 protein level more significantly than did deficiency of the RPs in Group 2 (*t* test, $P = 4.2e{-}07$; Figure 4D). In addition, in our RNA-seq data, we found more p53 target genes (53) showing elevated mRNA levels after knockdown of RPs in Group1 than after knockdown of RPs in Group 2 (*t* test, $P = 1.657e{-}15$; Figure 4E). Of note, our RNA-seq and Ribo-seq data showed that the transcriptional and translational changes in *TP53* gene expression after RP deficiency were minor, mainly <2-fold (Supplementary Figure S4E), suggesting that RP deficiency very likely regulates p53 abundance and activity at the protein level. We also found that the set of RPs affecting genes associated with the cell cycle/p53 signaling pathways upon knockdown were predominantly enriched with RPs entering the ribosome biogenesis pathway in the nucleus (hypergeometric test for all RPs, $P = 0.00034$; Supplementary Figure S4F). We further experimentally tested whether genomic depletion of the Group 1 RPs had a larger impact on cell growth than genomic depletion of Group 2 RPs by CRISPR-Cas9 experiments (see Methods) (54). Our CRISPR-Cas9 knockout data showed a significant correlation with that from the DepMap A549 dataset (Pearson

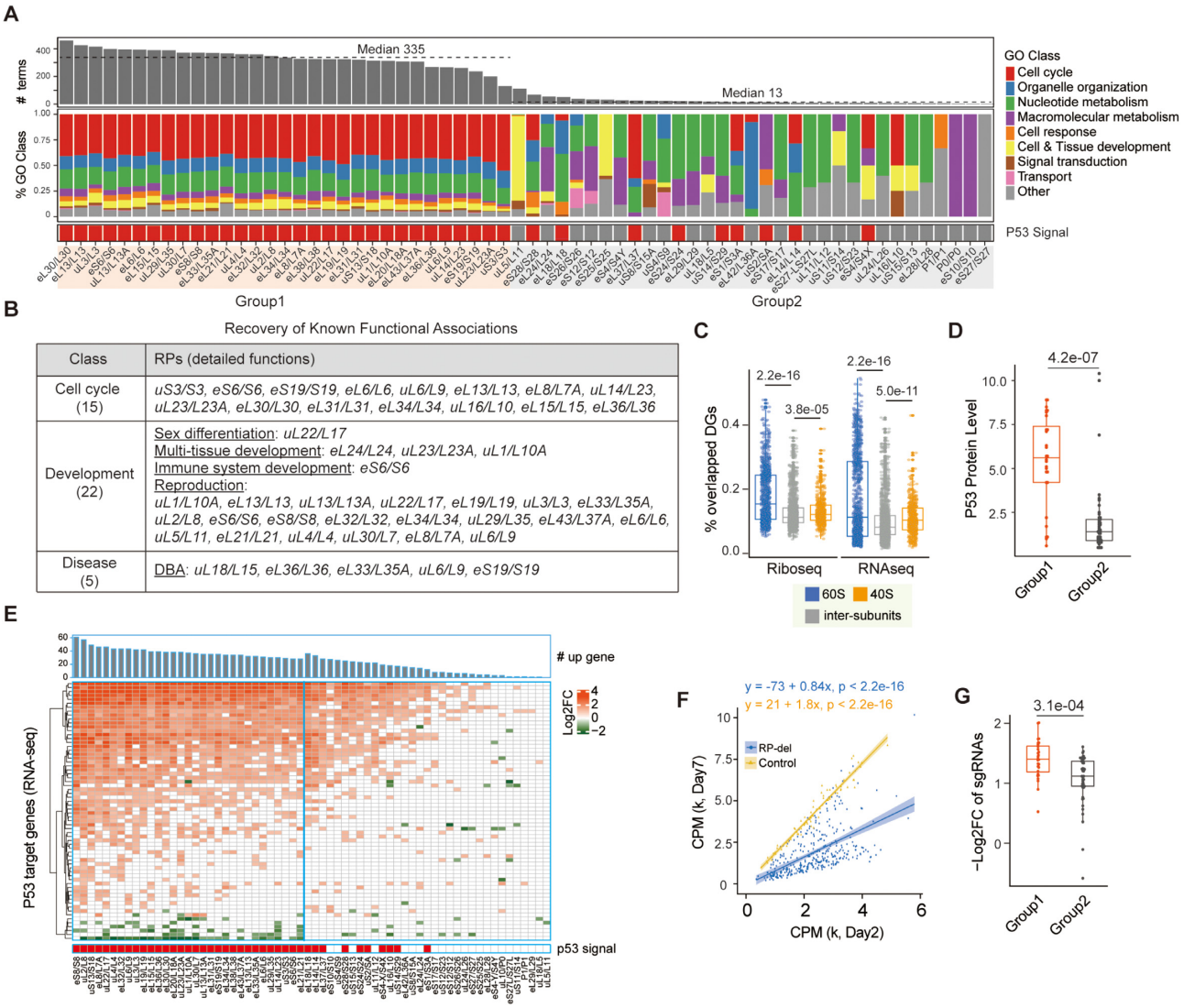

Figure 4. Functional characterization of molecular landscape of RP-deficient cells. (**A**) 64 RPs are ranked according to the number of significantly enriched GO BP terms. Annotation bar at the bottom indicates the enrichment of p53 signaling pathway after RP knockdown; Middle heatmap shows the fraction of GO classes; Bar plot at the top shows total number of enriched GO BP terms for each RP. (**B**) Summary of the recovered known functional associations of RPs. Details can be found in Supplementary Table S5. (**C**) Percentages of overlapped DEGs or DTGs after knockdown of 40S or 60S RPs. T-tests were performed. (**D**) Comparison of P53 protein levels after knockdown of Group1 and Group2 RPs. P53 protein levels were extracted from (42). (**E**) mRNA changes of p53 target genes in our RNA-seq datasets for the RPs in group1 and group2. The p53 target genes were extracted from *M Fischer*'s review (53). (**F**) Comparison of sgRNA expression levels at Day 2 and Day 7 after transfection. Linear regression models were estimated and tested for sgRNAs with RP targets and without targets. The estimated slope values indicate cell growth rate over time: slope >1 indicates positive cell growth, slope <1 indicates repressed cell growth. (**G**) Comparison of expression changes over time between sgRNAs targeting RPs from Group1 and that from Group2. *T*-test was performed.

correlation analysis, $r = 0.46$, $P = 3.773e{-}05$; Supplementary Figure S4G). As expected, the growth of cells transfected with RP-targeting sgRNAs was inhibited (*F* test, slope = 0.84, $P < 2.2e{-}16$), while the growth of cells transfected with nontargeting sgRNAs increased over time (*F* test, slope = 1.8, $P < 2.2e{-}16$; Figure 4F). Further comparison of the fold changes in RP-targeting sgRNAs revealed that disruption of Group 1 RPs inhibited cell growth more significantly than did disruption of Group 2 RPs (*t* test, $P = 3.1e{-}04$; Figure 4G), showing the greater inhibitory effects of Group 1 RP deficiency than Group 2 deficiency on cell growth and viability.

RP deficiency leads to divergent cell fates after cell cycle arrest

Our analysis showed that deficiency of many RPs perturbed the cell cycle and related pathways. We selected five RPs (*eS8/RPS8*, *eL13/RPL13*, *eL18/RPL18*, *eL22/RPL22* and *eL29/RPL29*) to validate their effects on cell cycle progression and cell proliferation upon mRNA knockdown. Among these RPs, *eS8/RPS8*, *eL13/RPL13* and *eL18/RPL18* were associated with the cell cycle in our analyses while *eL22/RPL22* and *eL29/RPL29* were not. Notably, the association of *eS8/RPS8* and *eL18/RPL18* with the cell cycle has not been previously reported.

Transfection of siRNAs targeting *eS8/RPS8*, *eL13/RPL13*, *eL18/RPL18*, *eL22/RPL22* or *eL29/RPL29* resulted in significant reductions in the corresponding mRNA and protein levels by more than 90% and by 36.7%∼77.3%, respectively, indicating the high knockdown efficiency (Supplementary Figure S5A, B). Flow cytometric analyses revealed that deficiency of *eS8/RPS8, eL13/RPL13* or *eL18/RPL18* significantly increased the G1-phase populations and decreased the S-phase population 24 h post treatment (t test, $P < 0.001$ for all three RPs), suggesting possible G1 arrest. On the other hand, knockdown of *eL22/RPL22* or *eL29/RPL29* did not change the cell cycle distribution in comparison to that in control cells (t test, $P > 0.05$; Figures 5A and Supplementary Figure S5C). Consistent with these findings, knockdown of *eS8/RPS8, eL13/RPL13* or *eL18/RPL18* significantly inhibited cell proliferation to various degrees in MTT assays at 72 h after siRNA transfection (t test, $P < 0.01$ for all three RPs; Figure 5B). In contrast, *eL22/RPL22* and *eL29/RPL29* had little impact on cell proliferation, and no difference was observed in cells lacking *eL22/R*PL22 or *eL29/RPL2*9 72 h posttransfection in comparison with that in control cells (*t* test, $P > 0.05$). Of note, we also examined the cellular phenotype after knockdown of *eL22/R*PL22 or *eL29/RPL2*9 in another tumor cell line, U2OS, and observed no change in the cell cycle distribution under our experimental conditions (Supplementary Figure S5D), which were consistent with the previous studies on the *eL22/R*PL22-deficient U2OS cells (55) and *eL29/RPL2*9-deficient HEK293 cells (56).

To elucidate the underlying mechanism, the protein levels of p53 and p21, two well-known cell cycle regulators (57,58), were examined by western blot analysis. As expected, the protein levels of p53 and p21 in cells lacking *eL22/RPL22* or *eL29/RPL29* showed no change compared to those in control cells. In contrast, the levels of p53 and p21 were elevated in cells lacking *eS8/RPS8, eL13/RPL13* or *eL18/RPL18* (*t* test, $P < 0.05$ for all three RPs (p53) and $P < 0.01$ for all three RPs (p21); Figure 5C). Moreover, although knockdown of all three RPs led to an increase in p21 expression to similar degrees, the protein levels of p53 appeared to be different, suggesting that cell cycle arrest after RP deficiency could be mediated through different mechanisms.

It is well known that increased p21 protein levels lead to different cellular consequences: senescence or apoptosis (59). To further explore possible cell fates determined by knockdown of *eS8/RPS8*, *eL13/RPL13* or *eL18/RPL18*, we performed TUNEL and SA-β-gal staining assays. Interestingly, we observed more TUNEL-positive nuclei in cells lacking *eS8/RPS8* than in control cells at 72 h after siRNA transfection (*t* test, $P < 0.05$), suggesting stimulation of apoptosis in these cells (Figures 5D and Supplementary Figure S5F). In contrast, we observed a gradual increase in β-gal-positive cells over time from 48 to 72 h after knockdown of *eL13/RPL13* (*t* test, $P < 0.01$) or *eL18/RPL18* (*t* test, $P < 0.01$), suggesting that an increase in senescence events was induced by deficiency of *eL13/RPL13* or *eL18/RPL18* (Figures 5E and Supplementary Figure S5G). Collectively, our results showed that depletion of different RPs influenced the cell cycle and cell fate through different pathways.

RP deficiency confers different functional preferences during development

Accumulating studies have emphasized the involvement of RP expression heterogeneity in specific cellular functions and developmental phenotypes (10,11,13). Our analysis indicated that RP deficiency changed the expression of genes associated with development in a wide range of tissues and organs, including those in the cardiovascular, respiratory, digestive, urogenital, reproductive and nervous systems (Supplementary Figure S6A). By western blot analysis of A549 cells lacking *uL5/RPL11* or *eL22/RPL22*, we validated changes in the protein expression of SOX9 and FOXO1, as examples of selected key molecules associated with development. SOX9 plays a central role in neural system development (60,61), while FOXO1 is an important regulator of cell growth that couples metabolic and proliferative activities (62,63). We showed that SOX9 and FOXO1 protein levels were significantly decreased in cells lacking *uL5/RPL11* but remained unchanged in cells lacking *eL22/RPL22* (Supplementary Figure S6B), which was consistent with our Riboseq data. Notably, some development-relevant functions of RPs have been previously reported. For example, our data showed that *uL22/RPL17* deficiency impacted genes related to sex differentiation, consistent with the observation that *uL22/RPL17* was differently expressed in the brains of male and female zebra finches during development (64). Deficiency of *eL24/RPL24*, *uL23/RPL23A* or *uL1/RPL10A* affected genes involved in embryonic development, consistent with the phenotypes of their mutants in developing embryos of zebrafish (65,66) and mice (67). On the other hand, we also identified previously unreported specific preferential perturbations in molecules related to tissue development conferred by a lack of certain RPs, among which were *uL5/RPL11*, whose deficiency was associated with neurogenesis, and *eL15/RPL15,* whose deficiency was associated with angiogenesis (Figure 6A).

To validate the phenotypic association of *uL5/RPL11* deficiency with neurogenesis, we coelectroporated a GFP plasmid together with RP-targeting short hairpin RNAs (shRNAs) into mouse retinas at P0 (postnatal day 0) and collected them at P12. The proportions of GFP-positive progeny distributed in different retinal cell layers at P12 were quantified. We observed significantly fewer Pax6-positive amacrine cells (*t* test, $P < 0.05$) and Chx10-positive bipolar cells (*t* test, $P < 0.01$) in the retinas of *uL5/Rpl11*-knockdown mice than in the retinas of control mice. In contrast, transfection of *uL5/R*pl11 shRNA increased the percentage of Sox9-positive Müller cells (*t* test, $P < 0.01$) and had no effect on the differentiation of Recoverin-positive photoreceptors (Figures 6B, C). We also tested *eL29/Rpl29,* which had no effect on neurogenesis, in our analysis as a negative control. As expected, we did not observe any changes in any of the cell subtypes from retinas of *eL29/Rpl29*-knockdown mice (Figures 6B, C). These results indicated that *uL5/Rpl11* deficiency inhibited retinal cell differentiation into amacrine and bipolar cells but promoted retinal cell differentiation into Müller cells.

To validate the cellular effects of *eL15/RPL15* deficiency on angiogenesis, we first tested the changes in the mRNA expression of several angiogenesis-associated genes, includ-

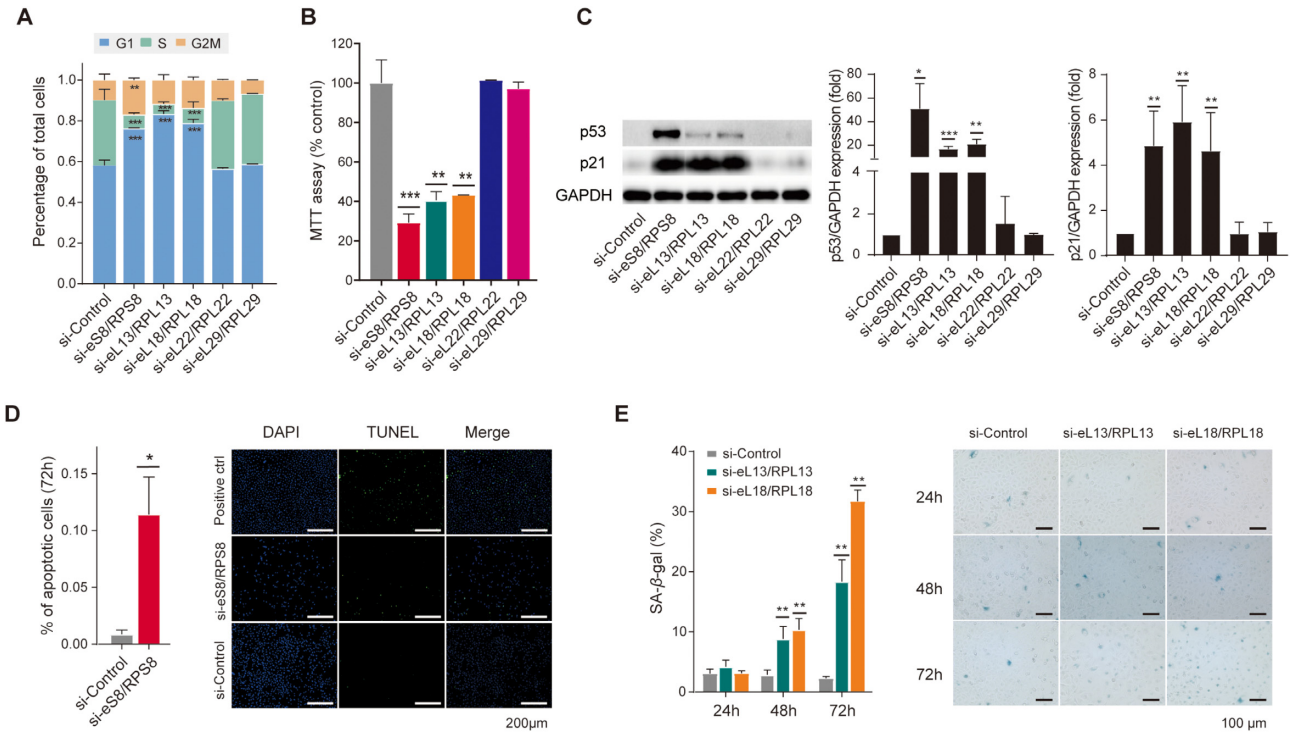

Figure 5. RP deficiency leads to divergent cell fates after cell cycle arrest. (**A**) Percentages of cells within different cell cycle stages (G1, S, and G2/M) by flow cytometry experiments on A549 cells at 24 h after knockdown of indicated RPs. Three replicates were used in *t*-tests. (**), $P < 0.01$; (***), $P < 0.001$. (**B**) Changes of cell viability by MTT assays on A549 cells at 24 h after knockdown of indicated RPs. Three replicates were used in t-tests. (**), $P < 0.01$; (***), $P < 0.001$. (**C**) Representative of western blotting assays (left panel) and quantification of p53 (middle panel) or p21 (right panel) protein levels at 24 h after knockdown of indicated RPs ($n = 2$ for p53 or 3 for p21 tests). T-tests were used. (*), $P < 0.05$; (**), $P < 0.01$; (***), $P < 0.001$. (**D**) Bar plots (left panel) showing the percentage of TUNEL+ cells at 72 h after knockdown of *eS8/RPS8*. Representative of TUNEL staining assays (right panel) for testing apoptosis *in situ* in A549 cells at 72 h after knockdown of *eS8/RPS8*. Three replicates were used in *t*-test. (*), $P < 0.05$. (**E**) Bar plots (left panel) showing the percentages of β-gal-positive cells at 24, 48 and 72 h after knockdown of *eL13/RPL13* or *eL18/RPL18*. Representative of β-gal staining assays (right panel) for testing senescence in A549 cells at 24, 48 and 72 h after knockdown of *eL13/RPL13*or *eL18/RPL18*. Three replicates were used in *t*-tests. (**), $P < 0.01$.

ing *BMPR2*, *C3*, *CAV1*, *MDM2*, *RIN2* and *VEGFA*, by real-time PCR. As expected, the mRNA levels of *BMPR2*, *C3*, *CAV1*, *MDM2* and *RIN2* were increased, but that of *VEGFA* was decreased upon *eL15/RPL15* knockdown (*t* test, all $P < 0.05$; Figure 6D), consistent with our sequencing data. *VEGFA* is known to be one of the most important proangiogenic factors and can be secreted by many types of cells, including diverse cancer cells and endothelial cells, to promote blood vessel growth (25). We also confirmed that the mRNA level of *VEGFA* was decreased in human umbilical vein endothelial cells (HUVECs) when *eL15/RPL15* was knocked down (*t* test, $P < 0.05$; Figure 6E). In addition, VEGFA protein secretion from *eL15/RPL15*-deficient cells was significantly decreased, as determined by ELISA (*t* test, $P < 0.01$; Figure 6F). To further determine the phenotypic impact of *eL15/RPL15* deletion, we knocked down this gene in HUVECs and performed a migration assay. The results showed that in comparison with the control siRNA treatment, *eL15/RPL15* deficiency inhibited cell migration (*t* test, $P < 0.05$; Figure 6G). Since VEGFA produced by tumor cells can promote angiogenesis to support their growth (68), we carried out experiments to simulate this condition. We treated HUVECs with conditioned medium (CM) from *eL15/RPL15*-deficient A549 cells and examined how the CM impacted cell migration and tube formation. We found no differences in migration and tube formation between HUVECs treated with CM from *eL15/RPL15*-deficient A549 cells and HUVECs treated with CM from control cells (Supplementary Figure S6B–D), suggesting that the effects of decreased *VEGFA* expression might be offset by increased expression of other proangiogenic factors by *eL15/RPL15* deficiency. Collectively, these results demonstrated that *eL15/RPL15* deficiency impacted the expression of *VEGFA* and its potential role in angiogenesis by affecting the migration of endothelial cells.

DISCUSSION

Our study represents the first systematic effort to study human RPs at multiple levels, including the global mRNA abundance (RNA-seq), the translation efficiency (Ribo-seq), and numerous genetic (CRISPR-Cas9 knockout) and phenotypic changes, after repression of individual RPs with specific siRNAs. In the present study, the RPF and RNA reads in all the analyses displayed the expected distribution and characteristics. Both the Ribo-seq and RNA-seq analyses were highly reproducible. Many molecular changes and cellular impacts conferred by RP deficiency were also consistent with those reported in previous studies and publicly available datasets. Thus, as a data collection effort, our

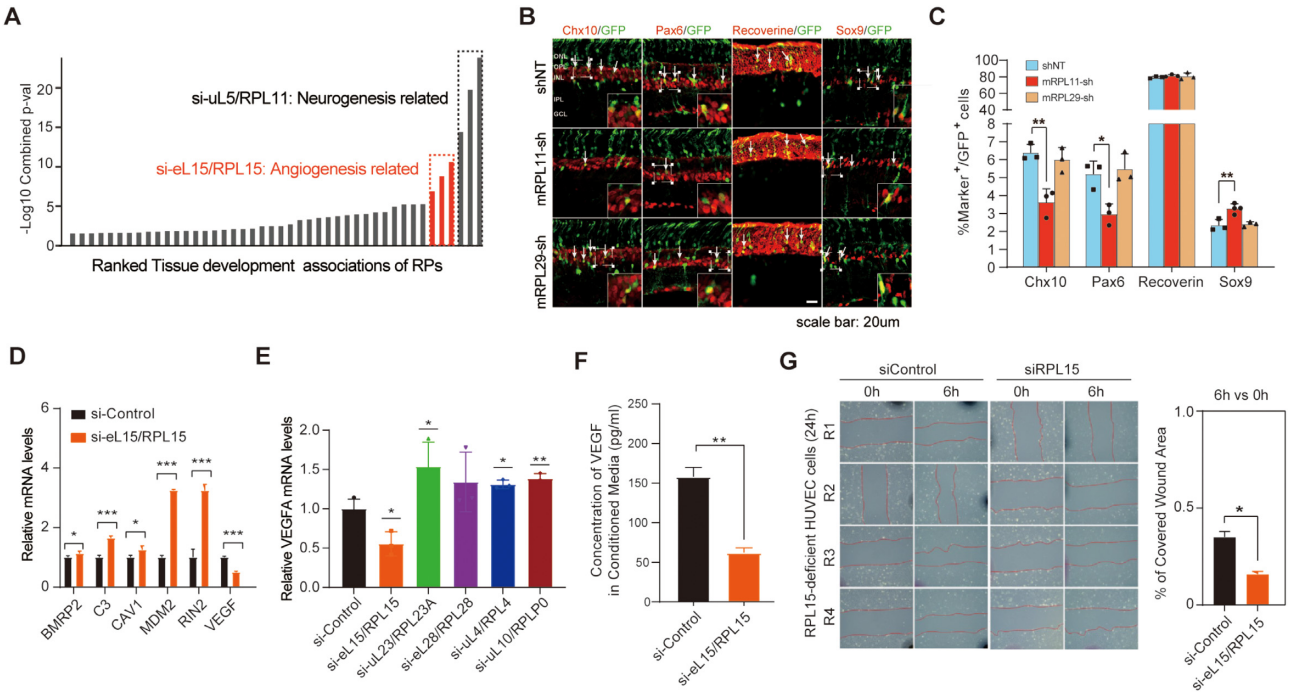

Figure 6. RP deficiency conferred different functional preference in development. (**A**) The ranked tissue development terms affected by RP knockdown according to the significance. Tissue development terms were defined according to GO structure. The p-values for all subentries belonging to the term of interest were combined with Fisher's method. Grey bars indicate GO terms enriched by down-DTGs; Red bars indicate GO terms enriched by up-DTGs. (**B**, **C**) Analysis of developing retinal cells after *in vivo* conditional knockdown of mouse *uL5/Rpl11*. (B) P0 retinas co-electroporated RP-targeting shRNAs or pU6 plasmid with the pCIG vector were collected at P12, and their sections were double-immunostained with an anti-GFP antibody and antibodies against Chx10, Pax6, Sox9 or Recoverine. Arrows point to representative colocalized cells. (C) The numbers of specific cell types and statistical testing results between groups. Two or three replicates were used in *t*-tests. (*), $P < 0.05$; (**), $P < 0.01$. (**D**) The relative mRNA levels by qPCR of representative genes in *eL15/RPL15*-deficient A549 cells. Three replicates were used in *t*-tests. (*), $P < 0.05$; (**), $P < 0.01$; (***), $P < 0.001$. (**E**) The relative mRNA levels of VEGFA in the control HUVEC and the HUVEC upon knockdown of indicated RPs. Three replicates were used in t-tests. (*), $P < 0.05$. (**F**) ELISA analysis showing the concentration of VEGF proteins in conditioned media from the control A549 cells and *eL15/RPL15*-deficient A549 cells. *T*-test was used. (**), $P < 0.01$. (**G**) Images of the control HUVEC and *eL15/RPL15*-deficient HUVEC 0hr and 6hr after a scratch was introduced in the monolayer with a pipette tip (left panel). The percentage of covered wound area for each replicate at 6 h over that at 0hr was estimated and compared between *eL15/RPL15*-deficient cells and the control cells (right panel). Four replicates were used in *t*-test. (*), $P < 0.05$.

study provides a massive and comprehensive data resource with high quality.

Our data demonstrated that RP deficiency led to substantial gene expression changes, with the effect of each RP varying to different degrees. Notably, we observed more dramatic changes in translation than in transcription after RP knockdown in most cases. This result showed that deficiency of a specific RP exerts less feedback on gene expression (i.e. mRNA transcription) than on the ability of ribosomes to translate specific mRNAs within the timeframe monitored in this study. This observation is consistent with Prof. Barna and colleagues' findings (7,15) and adds support to the ideas (i) that ribosomes that lack specific RPs can continue to translate mRNAs and (ii) that ribosomes lacking specific RPs can translate some mRNAs more/less effectively than others. While this result does not prove the existence of specialized ribosomes, it does demonstrate that ribosomes lacking specific RPs show preferences for certain classes of mRNAs.

Our data also demonstrated that the 60S RPs were functionally different from the 40S RPs in many aspects. Individual deficiency of 60S and 40S RPs resulted in distinct regulation of the nontargeted RPs at the levels of transcription, translation, and ribosome assembly. In addition, 60S RP deficiency usually resulted in more gene expression changes and more frequent upregulation of genes downstream of p53 signaling. This is consistent with the observation that depletion of 60S RPs can increase p53 protein levels more significantly than depletion of 40S RPs (42). We also observed that genetic depletion of RPs from the 60S subunit had a stronger inhibitory effect on cell growth. One possible explanation for these observations is the involvement of the RP–MDM2–p53 pathway (69,70). Individual depletion of RPs at the mRNA level in the present study directly led to ribosomal stress, resulting in an imbalance in free 60S and 40S subunits, as shown by our sucrose gradient analysis of ribosomal profiles for several selected RPs (Figure 3E). Previous studies revealed that perturbation of ribosome biogenesis contributes to nuclear stress, during which the excess free RP proteins, such as *uL18/RPL5* (71), *uL5/RPL11* (72), *uL14/RPL23* (73) and *uL24/RPL26* (74), that fail to be incorporated into ribosomal subunits can directly bind to MDM2 and, in turn, inhibit p53 ubiquitination, thus promoting p53 stability and accumulation, ultimately resulting in activation of p53 signaling.

By correlating the RPs included in the present study with ribosome biogenesis stages, we showed that the RPs affecting genes with a larger cellular impact and associated

with the cell cycle/p53 signaling pathways upon knockdown were mainly enriched with RPs entering the ribosome biogenesis pathway in the nucleus (Supplementary Figure S4F). Consistent with this finding, our data revealed that deficiency of several RPs located near or at the mRNA-binding channel in the ribosome (*RPS10, RPS20, RPS26, RPS31*) did not significantly affect genes in the cell cycle or p53 signaling pathway. These four RPs were assembled into ribosomes in the cytoplasm (2,75). In contrast, knockdown of the 40S subunit head-binding RPs (*eS10/RPS3, uS13/RPS18, eS19/RPS19*), which are required for export of nascent 40S subunits and are assembled into ribosomes early in their biogenesis, induced expression changes of genes enriched in the cell cycle and p53 signaling pathways. Regarding the RPs from 60S subunit, we also found that the RPs (*eL24/RPL24, eL29/RPL29, eL41/RPL41, P1/RPLP1* and *P2/RPLP2*) assembled in the late stage did not affect the cell cycle/p53 signaling pathways, even though all these RPs are located at the interface of the 40S and 60S subunits (75).

Our data also offer an opportunity for systematic investigation of *cis*-regulatory elements in mRNA targets, particularly in the 5′ UTRs. It is known that the 40S subunit is first recruited to the mRNA cap and the 60S subunit is then joined at the start codons (76). Based on this model, researchers have hypothesized that the translation of mRNAs containing elements blocking 40S scanning is sensitive to the 40S subunit concentration, while the translation of mRNAs with a poor Kozak context is sensitive to the 60S subunit concentration (77). We therefore explored the mRNA elements possibly involved in translational regulation after RP deficiency and found that knockdown of RPs from the 40S subunit usually decreased the TE of genes with a higher GC content in the 5′ UTRs, while knockdown of RPs from the 60S subunit usually increased the TE of genes with a strong Kozak sequence containing cytosine (C) bases at the –1 and –2 positions and a guanine (G) at the -3 position and decreased the TE of genes without these signals (Supplementary Figure S7). Further studies are required to explore the complex interactions between multiple *cis*-regulatory elements.

We presented several examples to demonstrate the value of our data in exploring novel regulatory roles and functions of RPs. We showed, for the first time, the suppressive effects of deficiency of eS8/*RPS8, eL13/RPL13* and eL18/*RPL18* on cell cycle progression in human cancer cells, suggesting an anticancer potential because targeting cell cycle pathway is considered to be an effective method for tumor suppression (78). We showed a novel physiological function of uL5/*RPL11,* whose knockdown *in vivo* induced dysregulation of neuronal differentiation in the retina. This finding extends our knowledge of the regulatory functions of *uL5/RPL11,* which was thought to be involved in DBA, as previous studies showed that partial loss of uL5/*RPL11* in adult mice can result in DBA-mimic phenotypes and predisposition to lymphomagenesis (79). Finally, we provided evidence of a novel role of *eL15/RPL15* in angiogenesis. We showed that eL15/*RPL15* deficiency preferentially affected angiogenic factors, including *VEGFA,* and found significant inhibitory effect on the migration of *eL15/RPL15*-deficient endothelial cells. While *eL15/RPL15* overexpression has been revealed to be associated with breast cancer metastasis (80), our data suggested that *eL15/RPL15* can also selectively regulate *VEGFA* to mediate cancer progression-related cellular functions. Further studies are required to test the functional significance of associations between RPs and other angiogenic factors in diverse human cancers.

DATA AVAILABILITY

All sequencing data were deposited to the Gene Expression Omnibus (GEO) with an accession number GSE168445, which will be publicly available upon the acceptance of the manuscript.

SUPPLEMENTARY DATA

Supplementary Data are available at NAR Online.

ACKNOWLEDGEMENTS

We would like to thank Dr Feng Zhang for providing helpful suggestions. We would also like to acknowledge the support from the Centre for Precision Medicine, Sun Yat-sen University.

Author contributions: Z.X. conceived and supervised the study. N.T. and JQ.Y. prepared sequencing libraries and performed high-throughput sequencing experiments. Y.Z.L. performed sequencing data processing, quality assessment and formal analysis. Y.W. and HW.W. helped sequencing data analysis. R.J., F.Z., N.T. and YZ.L. designed experiments on RPL15. N.T. and JQ.Y. performed experiments on RPL15. R.J. and MQ.X. supervised experiments on RPL15 and RPL11. YZ.L., N.T. and ST.L. designed mouse retina experiments. ST.L. and YN.G. performed mouse retina experiments. C.C.C. helped quality control analysis of sequencing datasets. Y.Z.L., N.T., J.Q.Y., S.T.L. and R.J. prepared the materials for the manuscript. Y.Z.L. and Z.X. wrote the manuscript. All authors read and approved the manuscript.

FUNDING

National Natural Science Foundation of China [31871302 to Z.X.]; Joint Research Fund for Overseas Natural Science of China [31829002 to Z.X.]; National Natural Science Foundation of China [31900477 to Y.Z.L.]. Funding for open access charge: National Natural Science Foundation of China [31900477 to Y.Z.L.].

Conflict of interest statement. None declared.

REFERENCES

1. Khatter,H., Myasnikov,A.G., Natchiar,S.K. and Klaholz,B.P. (2015) Structure of the human 80S ribosome. *Nature*, **520**, 640–645.
2. de la Cruz,J., Karbstein,K. and Woolford,J.L. Jr (2015) Functions of ribosomal proteins in assembly of eukaryotic ribosomes in vivo. *Annu. Rev. Biochem.*, **84**, 93129.
3. Klinge,S. and Woolford,J.L. Jr (2019) Ribosome assembly coming into focus. *Nat. Rev. Mol. Cell Biol.*, **20**, 116–131.
4. Bassler,J. and Hurt,E. (2019) Eukaryotic ribosome assembly. *Annu. Rev. Biochem.*, **88**, 281–306.
5. Natchiar,S.K., Myasnikov,A.G., Kratzat,H., Hazemann,I. and Klaholz,B.P. (2017) Visualization of chemical modifications in the human 80S ribosome structure. *Nature*, **551**, 472–477.

6. Panda,A., Yadav,A., Yeerna,H., Singh,A., Biehl,M., Lux,M., Schulz,A., Klecha,T., Doniach,S., Khiabanian,H. *et al.* (2020) Tissue- and development-stage-specific mRNA and heterogeneous CNV signatures of human ribosomal proteins in normal and cancer samples. *Nucleic Acids Res.*, **48**, 7079–7098.
7. Shi,Z., Fujii,K., Kovary,K.M., Genuth,N.R., Rost,H.L., Teruel,M.N. and Barna,M. (2017) Heterogeneous ribosomes preferentially translate distinct subpools of mRNAs Genome-wide. *Mol. Cell*, **67**, 71–83.
8. Ajore,R., Raiser,D., McConkey,M., Joud,M., Boidol,B., Mar,B., Saksena,G., Weinstock,D.M., Armstrong,S., Ellis,S.R. *et al.* (2017) Deletion of ribosomal protein genes is a common vulnerability in human cancer, especially in concert with TP53 mutations. *EMBO Mol. Med.*, **9**, 498–507.
9. Guimaraes,J.C. and Zavolan,M. (2016) Patterns of ribosomal protein expression specify normal and malignant human cells. *Genome Biol.*, **17**, 236.
10. Boria,I., Garelli,E., Gazda,H.T., Aspesi,A., Quarello,P., Pavesi,E., Ferrante,D., Meerpohl,J.J., Kartal,M., Da Costa,L. *et al.* (2010) The ribosomal basis of diamond-blackfan anemia: mutation and database update. *Hum. Mutat.*, **31**, 1269–1279.
11. Khajuria,R.K., Munschauer,M., Ulirsch,J.C., Fiorini,C., Ludwig,L.S., McFarland,S.K., Abdulhay,N.J., Specht,H., Keshishian,H., Mani,D.R. *et al.* (2018) Ribosome levels selectively regulate translation and lineage commitment in human hematopoiesis. *Cell*, **173**, 90–103.
12. Kondrashov,N., Pusic,A., Stumpf,C.R., Shimizu,K., Hsieh,A.C., Ishijima,J., Shiroishi,T. and Barna,M. (2011) Ribosome-mediated specificity in hox mRNA translation and vertebrate tissue patterning. *Cell*, **145**, 383–397.
13. Xue,S., Tian,S., Fujii,K., Kladwang,W., Das,R. and Barna,M. (2015) RNA regulons in hox 5' UTRs confer ribosome specificity to gene regulation. *Nature*, **517**, 33–38.
14. Chen,Y.X., Xu,Z.Y., Ge,X., Sanyal,S., Lu,Z.J. and Javid,B. (2020) Selective translation by alternative bacterial ribosomes. *Proc. Natl. Acad. Sci. U.S.A.*, **117**, 19487–19496.
15. Genuth,N.R. and Barna,M. (2018) The discovery of ribosome heterogeneity and its implications for gene regulation and organismal life. *Mol. Cell*, **71**, 364–374.
16. Farley-Barnes,K.I., Ogawa,L.M. and Baserga,S.J. (2019) Ribosomopathies: old concepts, new controversies. *Trends Genet.*, **35**, 754–767.
17. Chaudhuri,S., Vyas,K., Kapasi,P., Komar,A.A., Dinman,J.D., Barik,S. and Mazumder,B. (2007) Human ribosomal protein L13a is dispensable for canonical ribosome function but indispensable for efficient rRNA methylation. *RNA*, **13**, 2224–2237.
18. Ban,N., Beckmann,R., Cate,J.H., Dinman,J.D., Dragon,F., Ellis,S.R., Lafontaine,D.L., Lindahl,L., Liljas,A., Lipton,J.M. *et al.* (2014) A new system for naming ribosomal proteins. *Curr. Opin. Struct. Biol.*, **24**, 165–169.
19. McGlincy,N.J. and Ingolia,N.T. (2017) Transcriptome-wide measurement of translation by ribosome profiling. *Methods*, **126**, 112–129.
20. Schneider,C.A., Rasband,W.S. and Eliceiri,K.W. (2012) NIH image to imagej: 25 years of image analysis. *Nat. Methods*, **9**, 671–675.
21. Sui,G., Soohoo,C., Affar el,B., Gay,F., Shi,Y. and Forrester,W.C. (2002) A DNA vector-based RNAi technology to suppress gene expression in mammalian cells. *Proc. Natl. Acad. Sci. U.S.A.*, **99**, 5515–5520.
22. Subtelny,A.O., Eichhorn,S.W., Chen,G.R., Sive,H. and Bartel,D.P. (2014) Poly(A)-tail profiling reveals an embryonic switch in translational control. *Nature*, **508**, 66–71.
23. Sanson,K.R., Hanna,R.E., Hegde,M., Donovan,K.F., Strand,C., Sullender,M.E., Vaimberg,E.W., Goodale,A., Root,D.E., Piccioni,F. *et al.* (2018) Optimized libraries for CRISPR-Cas9 genetic screens with multiple modalities. *Nat. Commun.*, **9**, 5416.
24. Tsherniak,A., Vazquez,F., Montgomery,P.G., Weir,B.A., Kryukov,G., Cowley,G.S., Gill,S., Harrington,W.F., Pantel,S., Krill-Burger,J.M. *et al.* (2017) Defining a cancer dependency map. *Cell*, **170**, 564–576.
25. Kent,W.J., Sugnet,C.W., Furey,T.S., Roskin,K.M., Pringle,T.H., Zahler,A.M. and Haussler,D. (2002) The human genome browser at UCSC. *Genome Res.*, **12**, 996–1006.
26. Yates,A.D., Achuthan,P., Akanni,W., Allen,J., Alvarez-Jarreta,J., Amode,M.R., Armean,I.M., Azov,A.G., Bennett,R., Bhai,J. *et al.* (2020) Ensembl 2020. *Nucleic Acids Res.*, **48**, D682–D688.
27. D.obin,A., Davis,C.A., Schlesinger,F., Drenkow,J., Zaleski,C., Jha,S., Batut,P., Chaisson,M. and Gingeras,T.R. (2013) STAR: ultrafast universal RNA-seq aligner. *Bioinformatics*, **29**, 15–21.
28. Wang,L., Wang,S. and Li,W. (2012) RSeQC: quality control of RNA-seq experiments. *Bioinformatics*, **28**, 2184–2185.
29. Zhang,P., He,D., Xu,Y., Hou,J., Pan,B.F., Wang,Y., Liu,T., Davis,C.M., Ehli,E.A., Tan,L. *et al.* (2017) Genome-wide identification and differential analysis of translational initiation. *Nat. Commun.*, **8**, 1749.
30. van Heesch,S., Witte,F., Schneider-Lunitz,V., Schulz,J.F., Adami,E., Faber,A.B., Kirchner,M., Maatz,H., Blachut,S., Sandmann,C.L. *et al.* (2019) The translational landscape of the human heart. *Cell*, **178**, 242–260.
31. Liao,Y., Smyth,G.K. and Shi,W. (2014) featureCounts: an efficient general purpose program for assigning sequence reads to genomic features. *Bioinformatics*, **30**, 923–930.
32. Johnson,W.E., Li,C. and Rabinovic,A. (2007) Adjusting batch effects in microarray expression data using empirical bayes methods. *Biostatistics*, **8**, 118–127.
33. Leek,J.T., Johnson,W.E., Parker,H.S., Jaffe,A.E. and Storey,J.D. (2012) The sva package for removing batch effects and other unwanted variation in high-throughput experiments. *Bioinformatics*, **28**, 882–883.
34. Bercovich-Kinori,A., Tai,J., Gelbart,I.A., Shitrit,A., Ben-Moshe,S., Drori,Y., Itzkovitz,S., Mandelboim,M. and Stern-Ginossar,N. (2016) A systematic view on influenza induced host shutoff. *Elife*, **5**, e18311.
35. Gu,Z., Eils,R. and Schlesner,M. (2016) Complex heatmaps reveal patterns and correlations in multidimensional genomic data. *Bioinformatics*, **32**, 2847–2849.
36. Ashburner,M., Ball,C.A., Blake,J.A., Botstein,D., Butler,H., Cherry,J.M., Davis,A.P., Dolinski,K., Dwight,S.S., Eppig,J.T. *et al.* (2000) Gene ontology: tool for the unification of biology. The gene ontology consortium. *Nat. Genet.*, **25**, 25–29.
37. Kanehisa,M. (2019) Toward understanding the origin and evolution of cellular organisms. *Protein Sci.*, **28**, 1947–1951.
38. Kanehisa,M. and Goto,S. (2000) KEGG: kyoto encyclopedia of genes and genomes. *Nucleic Acids Res.*, **28**, 27–30.
39. Reimand,J., Kull,M., Peterson,H., Hansen,J. and Vilo,J. (2007) g:Profiler–a web-based toolset for functional profiling of gene lists from large-scale experiments. *Nucleic. Acids. Res.*, **35**, W193–W200.
40. Yu,G., Li,F., Qin,Y., Bo,X., Wu,Y. and Wang,S. (2010) GOSemSim: an r package for measuring semantic similarity among GO terms and gene products. *Bioinformatics*, **26**, 976–978.
41. Wang,J.Z., Du,Z., Payattakool,R., Yu,P.S. and Chen,C.F. (2007) A new method to measure the semantic similarity of GO terms. *Bioinformatics*, **23**, 1274–1281.
42. Nicolas,E., Parisot,P., Pinto-Monteiro,C., de Walque,R., De Vleeschouwer,C. and Lafontaine,D.L. (2016) Involvement of human ribosomal proteins in nucleolar structure and p53-dependent nucleolar stress. *Nat. Commun.*, **7**, 11390.
43. Barretina,J., Caponigro,G., Stransky,N., Venkatesan,K., Margolin,A.A., Kim,S., Wilson,C.J., Lehar,J., Kryukov,G.V., Sonkin,D. *et al.* (2012) The cancer cell line encyclopedia enables predictive modelling of anticancer drug sensitivity. *Nature*, **483**, 603–607.
44. Lorenz,R., Bernhart,S.H., Honer Zu Siederdissen,C., Tafer,H., Flamm,C., Stadler,P.F. and Hofacker,I.L. (2011) ViennaRNA package 2.0. *Algorithms Mol Biol*, **6**, 26.
45. U.,B., M.,P., H.E.,R. and M.,V. (eds.) (2007) In: *Structural Approaches to Sequence Evolution*. Springer, Berlin.
46. Ou,J., Wolfe,S.A., Brodsky,M.H. and Zhu,L.J. (2018) MotifStack for the analysis of transcription factor binding site evolution. *Nat. Methods*, **15**, 8–9.
47. Wagih,O. (2017) ggseqlogo: a versatile r package for drawing sequence logos. *Bioinformatics*, **33**, 3645–3647.
48. Weinberg,D.E., Shah,P., Eichhorn,S.W., Hussmann,J.A., Plotkin,J.B. and Bartel,D.P. (2016) Improved ribosome-footprint and mRNA measurements provide insights into dynamics and regulation of yeast translation. *Cell Rep.*, **14**, 1787–1799.

49. Wei,J., Kishton,R.J., Angel,M., Conn,C.S., Dalla-Venezia,N., Marcel,V., Vincent,A., Catez,F., Ferre,S., Ayadi,L. *et al.* (2019) Ribosomal proteins regulate MHC class i peptide generation for immunosurveillance. *Mol. Cell*, **73**, 1162–1173.
50. Gregory,B., Rahman,N., Bommakanti,A., Shamsuzzaman,M., Thapa,M., Lescure,A., Zengel,J.M. and Lindahl,L. (2019) The small and large ribosomal subunits depend on each other for stability and accumulation. *Life Sci. Alliance*, **2**, e201800150.
51. Robledo,S., Idol,R.A., Crimmins,D.L., Ladenson,J.H., Mason,P.J. and Bessler,M. (2008) The role of human ribosomal proteins in the maturation of rRNA and ribosome production. *RNA*, **14**, 1918–1929.
52. Ohtake,Y. and Wickner,R.B. (1995) KRB1, a suppressor of mak7-1 (a mutant RPL4A), is RPL4B, a second ribosomal protein L4 gene, on a fragment of saccharomyces chromosome XII. *Genetics*, **140**, 129–137.
53. Fischer,M. (2017) Census and evaluation of p53 target genes. *Oncogene*, **36**, 3943–3956.
54. Liu,Y., Cao,Z., Wang,Y., Guo,Y., Xu,P., Yuan,P., Liu,Z., He,Y. and Wei,W. (2018) Genome-wide screening for functional long noncoding RNAs in human cells by cas9 targeting of splice sites. *Nat. Biotechnol.***36**, 1203–1210.
55. Cao,B., Fang,Z., Liao,P., Zhou,X., Xiong,J., Zeng,S. and Lu,H. (2017) Cancer-mutated ribosome protein L22 (RPL22/eL22) suppresses cancer cell survival by blocking p53-MDM2 circuit. *Oncotarget*, **8**, 90651–90661.
56. Gopanenko,A.V., Kolobova,A.V., Meschaninova,M.I., Venyaminova,A.G., Tupikin,A.E., Kabilov,M.R., Malygin,A.A. and Karpova,G.G. (2020) Knockdown of the ribosomal protein eL29 in mammalian cells leads to significant changes in gene expression at the transcription level. *Cells*, **9**, 1228.
57. el-Deiry,W.S., Tokino,T., Velculescu,V.E., Levy,D.B., Parsons,R., Trent,J.M., Lin,D., Mercer,W.E., Kinzler,K.W. and Vogelstein,B. (1993) WAF1, a potential mediator of p53 tumor suppression. *Cell*, **75**, 817–825.
58. Levine,A.J. (1997) p53, the cellular gatekeeper for growth and division. *Cell*, **88**, 323–331.
59. Georgakilas,A.G., Martin,O.A. and Bonner,W.M. (2017) p21: a two-faced genome guardian. *Trends Mol. Med.*, **23**, 310–319.
60. Scott,C.E., Wynn,S.L., Sesay,A., Cruz,C., Cheung,M., Gomez Gaviro,M.V., Booth,S., Gao,B., Cheah,K.S., Lovell-Badge,R. *et al.* (2010) SOX9 induces and maintains neural stem cells. *Nat. Neurosci.*, **13**, 1181–1189.
61. Kang,P., Lee,H.K., Glasgow,S.M., Finley,M., Donti,T., Gaber,Z.B., Graham,B.H., Foster,A.E., Novitch,B.G., Gronostajski,R.M. *et al.* (2012) Sox9 and NFIA coordinate a transcriptional regulatory cascade during the initiation of gliogenesis. *Neuron*, **74**, 79–94.
62. Wilhelm,K., Happel,K., Eelen,G., Schoors,S., Oellerich,M.F., Lim,R., Zimmermann,B., Aspalter,I.M., Franco,C.A., Boettger,T. *et al.* (2016) FOXO1 couples metabolic activity and growth state in the vascular endothelium. *Nature*, **529**, 216–220.
63. Kim,D.Y., Hwang,I., Muller,F.L. and Paik,J.H. (2015) Functional regulation of foxo1 in neural stem cell differentiation. *Cell Death Differ.*, **22**, 2034–2045.
64. Tang,Y.P. and Wade,J. (2010) Sex- and age-related differences in ribosomal proteins L17 and L37, as well as androgen receptor protein, in the song control system of zebra finches. *Neuroscience*, **171**, 1131–1140.
65. Provost,E., Weier,C.A. and Leach,S.D. (2013) Multiple ribosomal proteins are expressed at high levels in developing zebrafish endoderm and are required for normal exocrine pancreas development. *Zebrafish*, **10**, 161–169.
66. Palasin,K., Uechi,T., Yoshihama,M., Srisowanna,N., Choijookhuu,N., Hishikawa,Y., Kenmochi,N. and Chotigeat,W. (2019) Abnormal development of zebrafish after knockout and knockdown of ribosomal protein L10a. *Sci. Rep.*, **9**, 18130.
67. Oliver,E.R., Saunders,T.L., Tarle,S.A. and Glaser,T. (2004) Ribosomal protein L24 defect in belly spot and tail (Bst), a mouse minute. *Development*, **131**, 3907–3920.
68. Apte,R.S., Chen,D.S. and Ferrara,N. (2019) VEGF in signaling and disease: beyond discovery and development. *Cell*, **176**, 1248–1264.
69. Macias,E., Jin,A., Deisenroth,C., Bhat,K., Mao,H., Lindstrom,M.S. and Zhang,Y. (2010) An ARF-independent c-MYC-activated tumor suppression pathway mediated by ribosomal protein-Mdm2 interaction. *Cancer Cell*, **18**, 231–243.
70. Wu,X., Bayle,J.H., Olson,D. and Levine,A.J. (1993) The p53-mdm-2 autoregulatory feedback loop. *Genes Dev.*, **7**, 1126–1132.
71. Dai,M.S. and Lu,H. (2004) Inhibition of MDM2-mediated p53 ubiquitination and degradation by ribosomal protein l5. *J. Biol. Chem.*, **279**, 44475–44482.
72. Zhang,Y., Wolf,G.W., Bhat,K., Jin,A., Allio,T., Burkhart,W.A. and Xiong,Y. (2003) Ribosomal protein L11 negatively regulates oncoprotein MDM2 and mediates a p53-dependent ribosomal-stress checkpoint pathway. *Mol. Cell. Biol.*, **23**, 8902–8912.
73. Dai,M.S., Zeng,S.X., Jin,Y., Sun,X.X., David,L. and Lu,H. (2004) Ribosomal protein L23 activates p53 by inhibiting MDM2 function in response to ribosomal perturbation but not to translation inhibition. *Mol. Cell. Biol.*, **24**, 7654–7668.
74. Zhang,Y., Wang,J., Yuan,Y., Zhang,W., Guan,W., Wu,Z., Jin,C., Chen,H., Zhang,L., Yang,X. *et al.* (2010) Negative regulation of HDM2 to attenuate p53 degradation by ribosomal protein L26. *Nucleic Acids Res.*, **38**, 6544–6554.
75. Anger,A.M., Armache,J.P., Berninghausen,O., Habeck,M., Subklewe,M., Wilson,D.N. and Beckmann,R. (2013) Structures of the human and drosophila 80S ribosome. *Nature*, **497**, 80–85.
76. Ramakrishnan,V. (2002) Ribosome structure and the mechanism of translation. *Cell*, **108**, 557–572.
77. Ferretti,M.B. and Karbstein,K. (2019) Does functional specialization of ribosomes really exist?*RNA*, **25**, 521–538.
78. Stewart,Z.A., Westfall,M.D. and Pietenpol,J.A. (2003) Cell-cycle dysregulation and anticancer therapy. *Trends Pharmacol. Sci.*, **24**, 139–145.
79. Morgado-Palacin,L., Varetti,G., Llanos,S., Gomez-Lopez,G., Martinez,D. and Serrano,M. (2015) Partial loss of rpl11 in adult mice recapitulates diamond-blackfan anemia and promotes lymphomagenesis. *Cell Rep.*, **13**, 712–722.
80. Ebright,R.Y., Lee,S., Wittner,B.S., Niederhoffer,K.L., Nicholson,B.T., Bardia,A., Truesdell,S., Wiley,D.F., Wesley,B., Li,S. *et al.* (2020) Deregulation of ribosomal protein expression and translation promotes breast cancer metastasis. *Science*, **367**, 1468–1473.